Geophysical Journal International

Geophys. J. Int. (2021) **225,** 906–925
Advance Access publication 2021 January 14
GJI Geodynamics and tectonics

doi: 10.1093/gji/ggab014

The interaction between mantle plumes and lithosphere and its surface expressions: 3-D numerical modelling

Yongming Wang and Mingming Li

School of Earth and Space Exploration, Arizona State University, Tempe, AZ, 85287*, USA. E-mail: wangym.ustc@gmail.com*

Accepted 2021 January 12. Received 2021 January 8; in original form 2020 June 21

SUMMARY

The rise of mantle plumes to the base of the lithosphere leads to observable surface expressions, which provide important information about the deep mantle structure. However, the process of plume–lithosphere interaction and its surface expressions remain not well understood. In this study, we perform 3-D spherical numerical simulations to investigate the relationship between surface observables induced by plume–lithosphere interaction (including dynamic topography, geoid anomaly and melt production rate) and the physical properties of plume and lithosphere (including plume size, plume excess temperature, plume viscosity, and lithosphere viscosity and thickness). We find that the plume-induced surface expressions have strong spatial and temporal variations. Before reaching the base of the lithosphere, the rise of a plume head in the deep mantle causes positive and rapid increase of dynamic topography and geoid anomaly at the surface but no melt production. The subsequent impinging of a plume head at the base of the lithosphere leads to further increase of dynamic topography and geoid anomaly and causes rapid increase of melt production. After reaching maximum values, these plume-induced observables become relatively stable and are more affected by the plume conduit. In addition, whereas the geoid anomaly and dynamic topography decrease from regions above the plume centre to regions above the plume edge, the melt production always concentrates at the centre part of the plume. We also find that the surface expressions have different sensitivities to plume and lithosphere properties. The dynamic topography significantly increases with the plume size, plume excess temperature and plume viscosity. The geoid anomaly also increases with the size and excess temperature of the plume but is less sensitive to plume viscosity. Compared to the influence of plume properties, the dynamic topography and geoid anomaly are less affected by lithosphere viscosity and thickness. The melt production significantly increases with plume size, plume excess temperature and plume viscosity, but decreases with lithosphere viscosity and thickness.

Key words: Mantle processes; Numerical modelling; Dynamics: convection currents and mantle plumes; Dynamics of lithosphere and mantle.

1 INTRODUCTION

Mantle plumes are buoyant upwellings that are likely generated from the thermal boundary layer at the bottom of the mantle (e.g. Morgan 1971; Morgan 1972). The mantle plume hypothesis has been widely accepted to account for several major observations that are not well explained by plate tectonics theory, such as the linear age progression of intraplate volcanism (e.g. Hawaiian-Emperor hotspot track), the formation of large igneous provinces (e.g. Deccan Traps and Siberian Traps), the unusually thickened crust at spreading centres (e.g. Iceland) and the geochemistry distinction between the mid-ocean ridge basalts and oceanic island basalts (e.g. Morgan 1971; Richards *et al.* 1989; Campbell & Griffiths 1990; Condie 2001; Davies 2001; Li *et al.* 2014). The partial melting caused by mantle plumes has also been suggested to be responsible for the origin and growth of continental crust (Condie 1998), and may play a critical role in the Earth's atmosphere evolution due to the release of volatiles during partial melting processes (e.g. Campbell & Kerr 2007).

In addition to Earth, mantle plumes have been suggested in other planets. Mantle convection models have shown that a single-plume thermal structure may develop dynamically in the Martian mantle (e.g. Harder & Christensen 1996; Roberts & Zhong 2006; Keller & Tackley 2009; Zhong 2009; Šrámek & Zhong 2012; Citron *et al.* 2018). The long history of volcanism in Tharsis and Elysium on Mars has been suggested to be caused by melting within the upwelling plumes, indicating a continuously active plume in these regions (e.g. Kiefer 2003; Li & Kiefer 2007). The volcanic rises

on Venus have been interpreted to indicate the presence of active mantle upwellings because of the associations with topographic highs, geoid highs, triple-junction rifting and large-scale magmatism (Kiefer & Hager 1991; Smrekar & Phillips 1991; Ernst & Desnoyers 2004; Smrekar *et al.* 2018). Through laboratory experiments, Davaille *et al.* (2017) showed that there may be plume-induced subduction on Venus which causes lithospheric deformation that is consistent with observations (Hansen 2002).

Although seismic observations have shown mantle plume structures in terms of lower-than-average seismic velocity anomalies in the deep mantle (Montelli *et al.* 2006; French & Romanowicz 2015; Nelson & Grand 2018), the precise physical properties (e.g. size, temperature and viscosity) of mantle plumes are difficult to constrain from seismic imaging and therefore remain unclear. The rise of mantle plumes to the base of the lithosphere changes the surface topography (Ribe & Christensen 1999; Zhong & Watts 2002), modifies the gravity observation (Ribe & Christensen 1999) and causes surface volcanism. Therefore, another approach to constrain the nature of mantle plumes is through examining these plume-induced surface expressions (e.g. Ribe & Christensen 1994; Ribe & Christensen 1999; Zhong & Watts 2002). However, the relationship between the physical properties of the mantle plume and the lithosphere and the surface expressions of plume–lithosphere interaction remains not well established.

Ribe & Christensen (1994) found that the best-fitting model to match the observed Hawaiian swell topography requires a plume with a radius of 90 km and an excess temperature of 300 °C. A later study by Zhong & Watts (2002) suggested that constraints from the swell geometry place a limit on the radius of the Hawaiian plume to be smaller than 70 km but with a higher plume excess temperature of $>$ 400 K. Farnetani & Richards (1994) found that the melt volume caused by the same plume could increase by about one order of magnitude if the lithosphere is allowed to undergo extension and thinning. The topographic features of plume–lithosphere interaction could also be significantly different due to variable rheological structure of the lithosphere (e.g. d'Acremont *et al.* 2003; Burov & Gerya 2014; King & Adam 2014). A single-plume structure of Mars has been proposed to be responsible for the massive volcanism in the Tharsis region and the geoid anomaly and topographic uplift as well (Harder & Christensen 1996; Harder 2000). Some studies, however, argued that at long wavelengths the plume buoyancy could only cause a fraction of the topographic uplift and geoid, and most of the current topography and geoid anomalies are probably due to volcanic construction of the lithosphere (Zhong 2002; Zhong & Roberts 2003; Roberts & Zhong 2004).

Numerical modelling experiments have also been carried out to constrain the interior structure of Venus by examining the surface observables due to plume–lithosphere interaction (e.g. Nimmo & McKenzie 1996; Smrekar & Parmentier 1996). The thickness of the thermal lithosphere estimated based on topography and gravity varies from approximately 100 to 300 km (e.g. Kiefer & Hager 1992; Nimmo & McKenzie 1996; Smrekar & Parmentier 1996) and the effective elastic thickness ranges from 10 to 50 km (Phillips 1994; Smrekar 1994). Smrekar & Parmentier (1996) proposed that model predictions of gravity, topography and melt volume could agree with observations with a near-surface plume excess temperature of 200 °C, a mantle temperature of 1300 °C and a plume duration of 75–175 Myr, although the plume temperature required to fit the observations depends on the plume life-span and the lithospheric thickness. Estimation of the relationship between the gravity and topography at highlands has also suggested the absence of the low-viscosity zone on Venus (e.g. Kiefer & Hager 1991; Huang *et al.* 2013) which has been suggested to exist on Earth (e.g. Richards & Hager 1984; Hager & Richards 1989).

The gravity anomaly, dynamic topography and melt production caused by plume–lithosphere interaction are strongly influenced by the physical properties of the plume and the lithosphere. However, it remains unclear to what extent the plume-induced geoid anomaly, dynamic topography and melt production are sensitive to the size, temperature, and viscosity of the plume, the thickness and viscosity of the lithosphere, and the depth-dependence of viscosity structure. In addition, previous geodynamic modelling studies have mostly focused on the steady-state stage of the plume–lithosphere interaction process, and it remains unclear how the surface expressions change with time during the plume–lithosphere interaction. In this paper, we perform 3-D spherical models to study the process of plume–lithosphere interaction featured by different stages including the rise of plume head in the deep mantle, the impinging of a plume head at the base of the lithosphere, and the interaction of a plume conduit with the lithosphere. By examining the time evolution of the plume-induced surface geoid anomaly, dynamic topography and melt production, we aim to build the connections between the physical properties of the plume and the lithosphere and the surface expressions induced by plume–lithosphere interaction.

2 METHODS

2.1 Model setup

We conduct regional spherical models by solving the non-dimensional equations for conservations of mass, momentum and energy under the Boussinesq approximation:

$$\nabla \cdot \vec{u} = 0 \tag{1}$$

$$-\nabla P + \nabla \cdot (\eta \dot{\varepsilon}) - RaT\,\hat{r} = 0 \tag{2}$$

$$\frac{\partial T}{\partial t} + (\vec{u} \cdot \nabla)\,T = \nabla^2 T + Q - L \tag{3}$$

where $\vec{u}$ is the velocity, P is the dynamic pressure, η is the viscosity, $\dot{\varepsilon}$ is the strain rate, Ra is the Rayleigh number, T is the temperature, $\hat{r}$ is the unit vector in the radial direction, t is the time, Q is the internal heating and L is the latent heating due to partial melting. The Rayleigh number is defined as:

$$Ra = \frac{\alpha \rho g_0 \Delta T R^3}{\kappa \eta_0} \tag{4}$$

where α, ρ, g_0, ΔT, κ, η_0 are dimensional parameters for the reference thermal expansivity, density, gravitational acceleration, temperature difference between the bottom and the surface, thermal diffusivity and viscosity, respectively. R is the radius of the Earth. Note that the Rayleigh number is defined using the radius of the Earth and is ∼10 times larger than that defined using the mantle thickness.

The conservation equations are solved using a modified finite-element code CitcomCU (Zhong 2006). To minimize the influence of side boundaries on mantle flow, the dimension of the computational domain is set as 90° × 90° × 1000 km, spanning from 0° E to 90° E and 45° S to 45° N (Fig. 1). The domain is divided into 256 × 256 × 96 elements in the horizontal and vertical directions, respectively.

Temperature is isothermal on the top ($T = 0$) and the bottom ($T = 1$). Thermal anomaly is imposed in the centre of the bottom

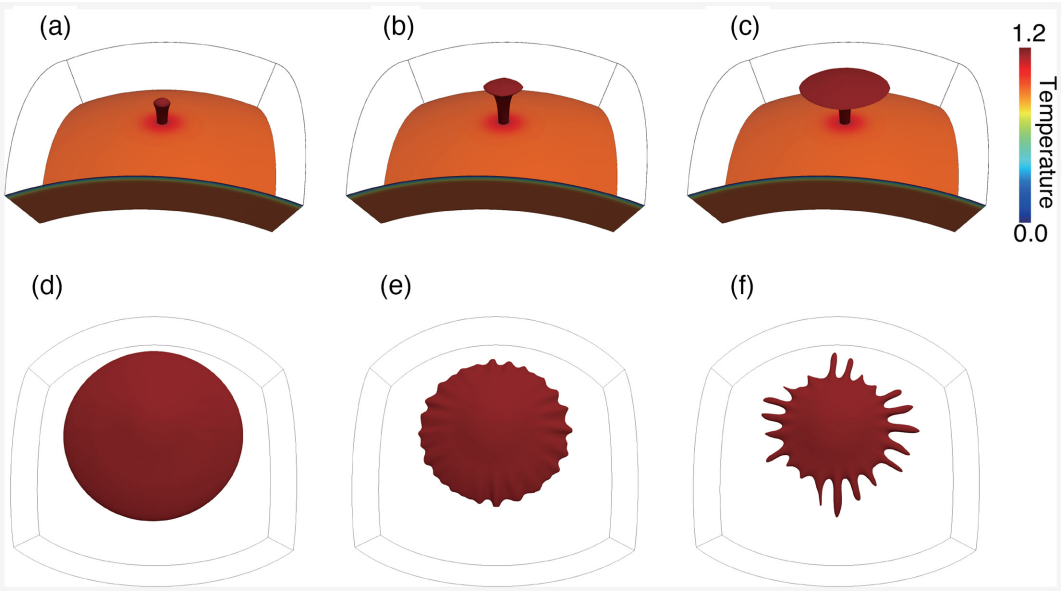

Figure 1. Parts (a)–(c) show three snapshots of the earlier stage of plume evolution for the reference case, case 1, at 9, 15 and 21 Ma, respectively. In (a)–(c), the plume is represented by red iso-surfaces with a non-dimensional residual temperature contour of $T = 0.2$, and the south side boundary shows the initial temperature structure. For better visualization, (a)–(c) only show the central part of the model domain with longitude of 22.5° E–67.5° E and latitude of 22.5° S–22.5° N. (d)–(f) show three snapshots of the later stage of plume evolution for case 1 at 75, 118 and 147 Ma, respectively. In (d)–(f), the spreading plume is represented by red iso-surfaces with a non-dimensional residual temperature (e.g. with the horizontally averaged temperature removed) contour of $T = 0.09$.

Table 1. Physical parameters of the numerical models.

Parameters	Value
Earth radius, R	6370 km
Model thickness, D	1000 km
Mantle density, ρ	3300 kg m^{-3}
Gravitational acceleration, g_0	9.8 m s^{-2}
Thermal expansivity, α	3×10^{-5} K^{-1}
Reference temperature, ΔT	1350 K
Reference viscosity, η_0	1.0×10^{21} Pa·s
Thermal diffusivity, κ	10^{-6} m^2 s^{-1}
Gas constant, $R_{\rm gas}$	8.31 J K^{-1} mol^{-1}

boundary to generate a plume at a fixed location (Fig. 1). The temperature anomaly of the plume exponentially decreases from plume centre to plume edge by $\Delta T = \Delta T_p \exp(-\frac{r^2}{R_p^2})$, where R_p and ΔT_p are the radius and excess temperature of the plume, respectively, and r is the distance from the plume centre. We use a non-dimensional internal heating rate of $Q = 100$ (e.g. a dimensional value of $\sim 4 \times 10^{-12}$ W kg^{-1}) in all models, but we expect the effect of internal heating to be small on a short timescale considered in this study (e.g. <200 Myr). The surface boundary is no-slip and the bottom boundary is stress-free. The side boundaries are insulating and free-slip. The initial temperature for the entire mantle is derived from a 1-D half-space cooling model with given lithospheric age. Since we focus on the interactions between mantle plume and the lithosphere, we only consider the upper-mantle dynamics, that is, the effects of lower-mantle flow on the dynamics of mantle plumes are not considered.

The viscosity is temperature-dependent and is given by $\eta = \exp[E(1.0 - T)]$, where E is the dimensionless activation energy. In some cases, a weak layer is introduced to the model domain beneath the lithosphere to study how it affects the surface expressions of plume–lithosphere interaction. All physical parameters of the numerical models are listed in Table 1.

2.2 Calculation of dynamic topography

The plume-induced dynamic topography at the surface (s) and the bottom (b) are derived from the radial stresses at the boundaries by:

$$s = \frac{\tau_{rr\_s} - \bar{\tau}_{rr\_s}}{\Delta\rho_s g_0} \tag{5}$$

$$b = \frac{\tau_{rr\_b} - \bar{\tau}_{rr\_b}}{\Delta\rho_b g_0} \tag{6}$$

where τ_{rr_s} and τ_{rr_b} are radial stress at the surface and the bottom, and $\bar{\tau}_{rr\_s}$ and $\bar{\tau}_{rr\_b}$ are the average values of τ_{rr_s} and τ_{rr_b}, respectively. $\Delta\rho_s$ and $\Delta\rho_b$ are density jumps across the surface and the bottom, respectively. Note that $\Delta\rho_s$ is essentially the density difference between mantle rock and air (as assumed in this study) or water (if ocean is considered). The radial stresses at the top and bottom boundaries are determined using the consistent boundary flux method, which has been shown to be more accurate than the standard pressure smoothing method (Zhong *et al.* 1993).

2.3 Calculation of geoid anomaly in regional model using an integration method

The anomaly of gravitational potential, φ, is often determined by solving the Poisson's equation:

$$\nabla^2\varphi = -4\pi G\delta\rho_{\rm total} \tag{7}$$

where G is the gravitational constant and $\delta\rho_{\rm total}$ represents the density anomalies due to mantle internal density variations as well as those associated with the topography at the surface and bottom. In full-spherical global convection models, the Poisson's equation is conventionally solved under the spectral domain using the spherical harmonic expansion method (Zhong *et al.* 2008). However, in

partial-spherical regional convection models, it is not straightforward to solve Poisson's equation with the tool of spherical harmonic expansions. Instead, in regional models we calculated the gravitational potential at each point on the surface by direct integrating the contributions from density anomalies within each element of the model domain and that due to the surface and bottom topography:

$$\varphi_f = \int_V \frac{G\delta\rho_f}{r} dV \tag{8}$$

$$\varphi_{s,b} = \int_V \frac{G\delta\rho_{s,b}}{r} dV \tag{9}$$

where φ_f and $\varphi_{s,b}$ are gravitational potential perturbations caused by internal density perturbation $\delta\rho_f$ and the density anomalies associated with the topography at the surface ($\delta\rho_s$) and the bottom ($\delta\rho_b$), respectively. dV is the volume of the element and r is the distance measured from the centre of the element to the observational point at the surface. The integration for φ_f is performed over the entire volume of the model elements, while the integration for $\varphi_{s,b}$ is performed over the surface and bottom boundary elements. The geoid anomaly is calculated by:

$$\delta N = \frac{\varphi}{g_0} \tag{10}$$

where g_0 is the reference gravitational acceleration (Table 1).

To benchmark the accuracy of this integration method, we first implemented it in the 3-D full spherical mantle convection code CitcomS, in which the spherical harmonic expansion method has already been implemented and benchmarked (Zhong *et al.* 2008). We chose a few models in Zhong *et al.* (2008) to reproduce their calculations and compare the geoid anomalies between our integration method and the spectral method. Fig. 2 shows the results for two benchmark cases, one with purely thermal convection (case C3 in Zhong *et al.* 2008) and the other with thermo-chemical convection (case D1a in Zhong *et al.* 2008). The results from our integration method show excellent agreement with that from the spherical harmonic expansion method, in both the pattern and the magnitude of the geoid anomalies (Fig. 2).

Fig. 3 shows the power spectrum of each geoid anomaly component for the thermal and thermo-chemical benchmark calculations. For a spherical harmonic degree l, the magnitude is defined as:

$$\Gamma_l = \sum_{m=0}^{l} \left[\left(f_{\cos}^{lm}\right)^2 + \left(f_{\sin}^{lm}\right)^2 \right] \tag{11}$$

where $f_{\cos}^{lm}$ and $f_{\sin}^{lm}$ are the cosine and sine coefficients at degree l and order m, respectively. Our integration method shows good agreement with that from the spectral method, especially for geoid components due to internal density anomaly and surface topography (Fig. 3). There are some discrepancies for geoid anomaly due to bottom topography at higher degrees when the magnitude is rather small (e.g. $<10^{-3}$, Fig. 3), which are caused by numerical artefacts due to limited model resolution. However, the amplitude of the geoid anomaly due to bottom topography is rather small compared to that from the internal density anomaly and surface topography and has little influence on the net geoid anomaly (Fig. 3).

2.4 Calculation of melt production rate

We used a similar approach as in Li *et al.* (2016) to calculate the melt production caused by plume–lithosphere interaction. The melt fraction, F, at each element of the computational domain is calculated using the parametrized melting equations developed by Katz *et al.* (2003) for given pressure (P) and temperature (T). Using the Euler method as described in Li *et al.* (2016), the melt production rate within an element is given by:

$$\frac{dM_{\text{melt}}}{dt} = M_{\text{rock}} \left(\frac{\partial F}{\partial t} + \vec{u} \cdot \nabla F \right) \tag{12}$$

where M_{melt} is the mass of melt produced in the element, t is time, M_{rock} is the total mass of mantle rock within the element, $\vec{u}$ is the mantle flow velocity and F is the melt fraction. The extraction of melts to the surface can only be triggered when $F > F_{\text{threshold}}$ and $\frac{dF}{dt} > 0$, where $F_{\text{threshold}}$ is a threshold of melt fraction above which melt extraction occurs. Previous studies suggested $F_{\text{threshold}}$ to be in the range of 0.01–0.04 (Spiegelman & McKenzie 1987; Forsyth *et al.* 1998; Connolly *et al.* 2009). In this study, we choose a melt extraction threshold of $F_{\text{threshold}} = 0.02$ in the middle of that range.

We use an anhydrous melting formulation that has been proposed by Katz *et al.* (2003). Because the adiabatic heating is removed in our models under the Boussinesq approximation, the adiabatic temperature is added back when calculating the melt fraction, and we apply an adiabatic temperature gradient of $0.4\,^{\circ}\text{C km}^{-1}$. The latent heating due to partial melting is assumed to be 640 KJ mol^{-1} (Navrotsky 1995). Like Li *et al.* (2016), the latent heating is treated as a heat sink in the equation of conservation of energy (eq. 3) and is removed with the extraction of melts.

3 NUMERICAL RESULTS

We have computed 23 cases with different physical parameters, including the plume radius R_p, the plume excess temperature ΔT_p and the lithosphere thickness D_l which is related to its age by $D_l = 2.32\sqrt{\kappa A_l}$ (e.g. the bottom of the lithosphere is defined by $T = 0.9$) and the presence of a weak-viscosity layer beneath the lithosphere. We varied the activation energy E for the temperature dependence of viscosity to build models with different plume and lithosphere viscosities. The parameters for all cases are summarized in Table 2.

3.1 Reference case

We first present the result of the reference case, case 1, which has $R_p = 300$ km, $\Delta T_p = 300\,^{\circ}\text{C}$, $D_l = 120$ km ($A_l = 80$ Ma) and $E = 6.91$ which gives rise to a 10^3 maximum viscosity variation between the lithosphere and the mantle (e.g. Zhong 2006). Fig. 4 shows a time evolution of the surface topography, the geoid anomaly and melt production due to the plume–lithosphere interaction. From $t = 0$ to ~15 Ma, the rising of a mantle plume to the base of the lithosphere (Fig. 1a) causes a topographic swell of a few kilometres at the surface above the plume head (Fig. 4a, column 1). The dynamic topographic uplift induces a positive geoid anomaly (Fig. 4a, column 2), while the thinning of the lithosphere and the excess plume temperature cause a negative geoid anomaly (Fig. 4a, column 3). The net geoid anomaly is positive above the plume head (Fig. 4a, column 4), because the contribution from the topography to geoid anomaly is larger than that from the internal density anomaly as the topography response is closer to the surface. No melt is produced by the plume before $t = 15$ Ma (Fig. 4a, column 5). Note that the bottom dynamic topography and its contribution to the geoid anomaly are zero, due to its stress-free boundary condition.

With time, the plume continues to rise to reach the base of the lithosphere and spreads out laterally beneath the lithosphere (Figs 1b and c). The continuous rising and spreading of the plume increase

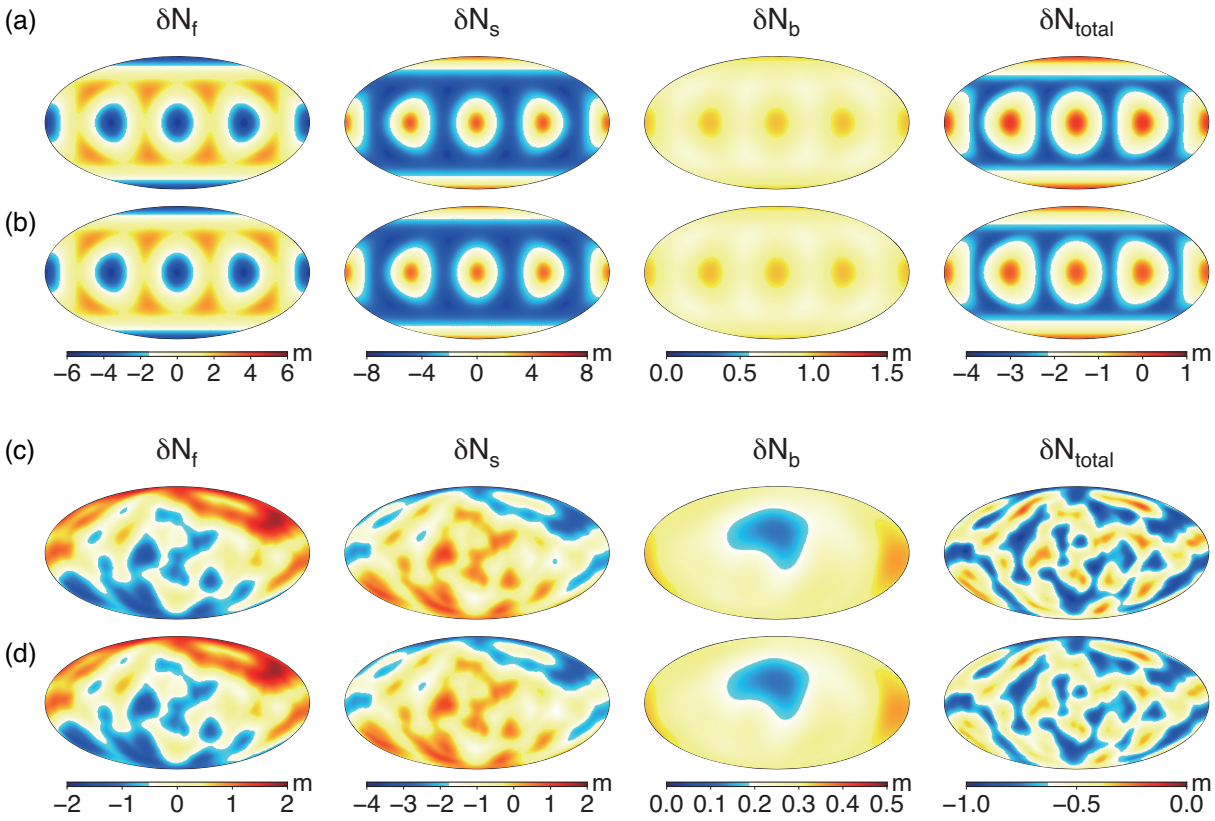

Figure 2. Comparison of methods to calculate geoid anomaly for two benchmark cases one (a) and (b) with purely thermal convection and (c) and (d) the other with thermo-chemical convection. (a) and (c) are geoid anomalies from integration method, (b) and (d) are geoid anomalies from spherical harmonic expansion method. In (a)–(d), the geoid anomaly contributions from internal density perturbation δN_f, and that associated with the surface topography δN_s and the bottom topography δN_b are shown separately.

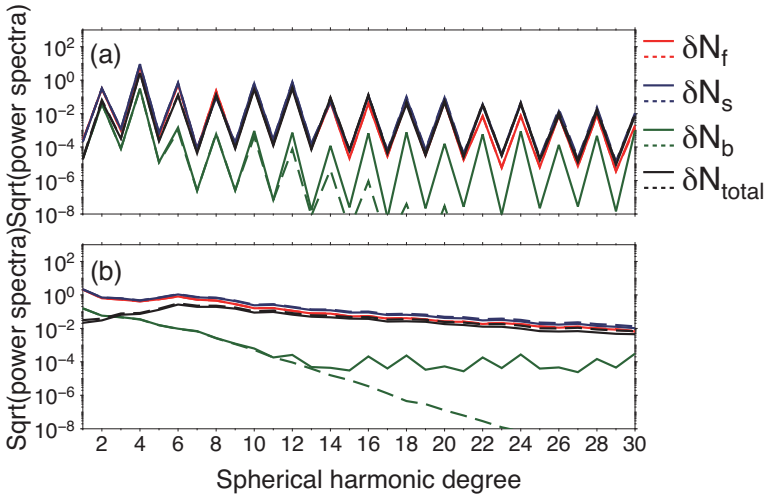

Figure 3. Comparison of the power spectra of the geoid anomalies calculated by integration method and spectral method, for (a) the thermal convection model case C3 in Zhong *et al.* (2008), and (b) the thermo-chemical convection model case D1a in Zhong *et al.* (2008). In (a) and (b), the solid lines denote results from the integration method and the dash lines denote results from the spectral method, respectively. δN_f (red), δN_s (blue) and δN_b (green) are the geoid anomaly caused by the internal buoyancy, the surface topography and the bottom topography, respectively.

the elevation of the swell topography above the plume and cause a larger area with topographic uplift (Figs 4b and c, column 1). The amplitudes of the positive geoid anomaly from topography (Figs 4b and c, column 2) and the negative geoid anomaly from internal density anomaly (Figs 4b and c, column 3) both increase with time. The net geoid anomaly remains positive due to the dominating role of topography contribution (Figs 4b and c, column 4). Meanwhile, partial melting starts to produce melt extraction to the surface which mainly occurs at the centre part of the plume head (Figs 4b and c, column 5).

Table 2. Input parameters and outputs of numerical models*.

Model	R_p (km)	ΔT_p (°C)	E_l	E_m	D_l (km)	H (km)[a]	N (m)[a]	GTR (m km^{-1})[a]	dM/dt (km^3 yr^{-1})[a]
case1	300	300	6.91	6.91	120	4.03(0.04)	176.8(0.63)	43.8(0.50)	0.29(0.02)
caseR1	**400**	300	6.91	6.91	120	4.30(0.08)	220.1(7.32)	51.2(0.77)	0.37(0.02)
caseR2	**200**	300	6.91	6.91	120	3.24(0.13)	107.8(4.20)	33.3(0.31)	0.14(0.04)
caseR3	**100**	300	6.91	6.91	120	1.46(0.21)	27.90(3.74)	19.2(0.28)	0.004(0.0024)
caseT1	300	**350**	6.91	6.91	120	4.32(0.02)	201.3(3.20)	46.6(0.49)	1.20(0.07)
caseT2	300	**250**	6.91	6.91	120	3.55(0.08)	147.3(1.30)	41.5(0.70)	0.013(0.007)
caseT3	300	**200**	6.91	6.91	120	2.89(0.10)	114.7(3.09)	39.8(0.63)	0.0(0.0)
caseL1	300	300	**11.5**	6.91	120	3.77(0.013)	174.8(0.72)	46.3(0.31)	0.11(0.015)
caseL2	300	300	**9.21**	6.91	120	3.86(0.02)	175.5(0.67)	45.5(0.37)	0.16(0.02)
caseL3	300	300	**4.61**	6.91	120	4.39(0.07)	178.1(0.63)	40.6(0.72)	0.71(0.02)
caseP1	300	300	6.91	**11.5**	120	3.70(0.04)	181.5(5.30)	49.1(0.89)	0.19(0.03)
caseP2	300	300	6.91	**9.21**	120	3.87(0.003)	179.3(2.50)	46.3(0.67)	0.23(0.02)
caseP3	300	300	6.91	**4.61**	120	4.17(0.06)	171.6(1.00)	41.2(0.45)	0.35(0.02)
caseE1	300	300	**11.5**	**11.5**	120	3.44(0.06)	180.1(5.29)	52.4(0.62)	0.034(0.012)
caseE2	300	300	**9.21**	**9.21**	120	3.70(0.014)	178.1(2.56)	48.2(0.51)	0.11(0.018)
caseE3	300	300	**4.61**	**4.61**	120	4.54(0.096)	173.5(0.93)	38.2(0.71)	0.75(0.04)
caseA1	300	300	6.91	6.91	**160**	4.33(0.084)	191.4(1.20)	44.2(0.66)	0.049(0.023)
caseA2	300	300	6.91	6.91	**140**	4.20(0.063)	184.5(0.88)	44.0(0.57)	0.13(0.03)
caseA3	300	300	6.91	6.91	**100**	3.93(0.028)	172.4(0.73)	43.8(0.45)	0.41(0.018)
caseW1[b]	300	300	6.91	6.91	120	3.42(0.022)	140.6(1.92)	41.1(0.30)	1.9(0.055)
caseW2[b]	300	300	6.91	6.91	120	2.66(0.037)	106.2(1.64)	40.0(0.07)	2.83(0.13)
caseW3[b]	300	300	6.91	6.91	120	2.77(0.045)	116.0(6.25)	42.0(2.83)	9.86(0.59)
caseW4[b]	300	300	6.91	6.91	120	1.30(0.087)	26.60(5.92)	20.3(3.22)	12.14(1.16)

[a]Average value of the dynamic topography, geoid anomaly and GTR at the plume centre and the total melt production rate between 40 and 80 Ma. The numbers in parentheses are standard deviations.
[b]These are cases with a weak layer beneath the lithosphere with different thickness and viscosity reduction.
*We vary the bold parameters with respect to case 1 to explore their effects on our results.

From 24 to 47 Ma, the plume head keeps spreading at the base of the lithosphere, causing more surface areas to have increased dynamic topography (Figs 4b and c, column 1). However, the amplitude of the swell topography at the centre part of the plume head (with a radius of 5°, i.e. ∼550 km from the plume centre) is relatively stable at ∼4 km (Fig. 4d), since the thinning of the lithosphere at this region has reached a thermally equilibrium state with the plume beneath it. However, the geoid contribution from the topography and the internal density anomaly at this region still increases significantly due to the contribution from regions outside of the plume centre (Figs 4e and f), resulting in a slight increase of the net geoid anomaly during this time period (Fig. 4g). The amount of partial melting produced by the plume also increases with time but is still concentrated in the central part of the plume head (Figs 4c and h).

After 47 Ma, the area with positive dynamic topography keeps increasing, but its magnitude around the plume centre remains unchanged (e.g. Fig. 4d, 47–75 Ma, a radius of 30° or ∼3000 km from the centre). The positive and the negative contributions to geoid anomaly respectively from the dynamic topography and the internal density anomaly both increase slightly, but the net geoid anomaly remains relatively unchanged near the centre part of the plume (Figs 4e–g). The melt production still concentrates at the plume centre and its rate becomes relatively stable after 47 Ma (Fig. 4h). It is also interesting to note that, at some later stage of plume–lithosphere interaction, small-scale convection develops at the edges of the plume head, leading to fingering structures with hotter and less viscous materials intruding into the surrounding colder and more viscous background mantle (Figs 1d–f), which is known as the Saffman–Taylor instability (Saffman & Taylor 1958).

The overall temporal and spatial evolution of the dynamic topography, geoid anomaly and geoid-to-topography ratio (GTR) for the reference case are shown in Fig. 5. The topography and geoid anomaly both decrease with the increasing distance from the plume centre (Figs 5a and b). At locations within ∼1000 km from the plume centre, the topography reaches its maximum at approximately 25 Ma and becomes relatively stable (Fig. 5a). Interestingly, at ∼1000–2000 km from the plume centre, the topography slightly decreases after it reaches its maximum (Fig. 5a), which is caused by small-scale convection developed beneath the lithosphere. The geoid anomaly therefore decreases at some later stage (e.g. after 100 Ma) due to the reduced contribution from topography even for the centre part above the plume (Fig. 5b).

The GTR is ∼40 m km^{-1} within ∼800 km from the plume centre and increases to ∼60 m km^{-1} in regions ∼1000–2000 km from the plume centre (Fig. 5c). Some unusual GTR appears at the edge of the plume head which is likely to be caused by the very small topography at the spreading margin. The GTR is much larger (∼70 m km^{-1}) before the plume head reaches the base of the lithosphere and decreases rapidly as the plume head starts to cause significant dynamic topography above it (Fig. 5d). Once the plume head has spread out at the base of the lithosphere, the GTR becomes relatively stable and slightly decreases with time, for example, with a reduction of ∼5 m km^{-1} from 50 to 200 Ma (Fig. 5d). The GTR at the centre point over the plume (Fig. 5d, red line) is smaller than the average GTR calculated from the whole area that is influenced by plume–lithosphere interaction (which is measured as the slope of the line that best fits the total geoid-topography data points based on the least-squares method) (Fig. 5d, blue line), but with a similar trend.

3.2 Influences of model parameters

In this section, we examine how plume radius, plume excess temperature, plume viscosity, lithosphere viscosity, lithosphere thickness and the weak layer control the time evolution of the geoid

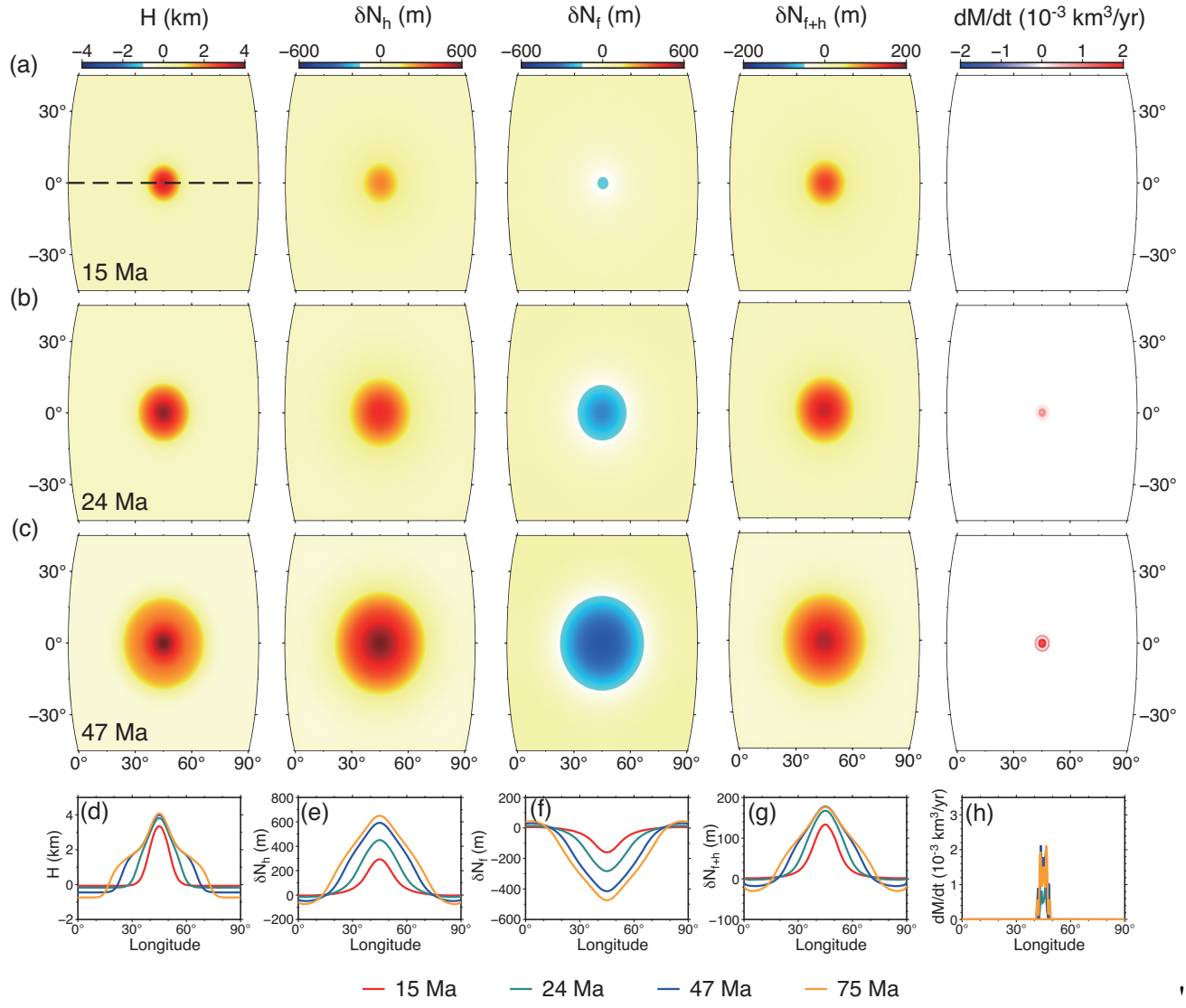

Figure 4. Evolution of topography, geoid anomaly and melt production rate at the surface for case 1. (a)–(c) are snapshots of surface topography (H), geoid anomaly from topography (δN_h), geoid anomaly from internal density anomaly (δN_f), total geoid anomaly (δN_{f+h}) and melt production rate (dM/dt) at 15, 24 and 47 Ma, respectively. (d)–(h) show the variation of H, δN_h, δN_f, δN_{f+h} and dM/dt at four different time snapshots over a cross line through the centre of the plume, that is, the black dash line in (a).

anomaly, surface topography, GTR and melt production rate due to the plume–lithosphere interaction. For simplicity, we focus on the dynamic topography, geoid anomaly and GTR at the plume centre, but the trend of their spatial variations is similar to the reference case as will be shown later. The melt production is shown as the summation across the model domain.

3.2.1 *Effects of plume radius*

In cases R1, R2 and R3 (Table 2), all other parameters are identical to the reference case (case 1) except the plume radius R_p changes to 400, 200 and 100 km, respectively. The spatial variations of the dynamic topography, geoid anomaly and GTR for these cases are similar to case 1, but their temporal variations are quite different (Fig. 6). For case R1 with $R_p = 400$ km the spreading of the plume has affected ~80 per cent of the surface area until ~75 Ma, while for case R3 with smaller plume of $R_p = 100$ km the plume only affects ~20 per cent of the surface area until 200 Ma (Fig. 6). Generally, a larger plume reaches the base of the lithosphere sooner and produces a larger geoid anomaly (Fig. 7a), a larger swell topography (Fig. 7b) and a larger GTR (Fig. 7c). Interestingly, when the plume radius is 400 km, the geoid anomaly and dynamic topography both decrease quickly after it reaches its maximum in the early 30 Ma (Figs 7a and b). This is because the plume spreads out beneath the lithosphere more quickly and the temperature at the base of the lithosphere is more homogenized than cases with smaller plume radius, which results in smaller spatial variations of geoid anomaly and dynamic topography. For all three models, the GTR first decreases rapidly before the plume reaches the base of the lithosphere and becomes relatively unchanged after the plume spreads out at the bottom of the lithosphere (Fig. 7c).

The melt production rate increases significantly with the increase of plume radius (Fig. 7d). For example, as the plume radius increases from 100 to 200 km, the total melt production rate is increased by

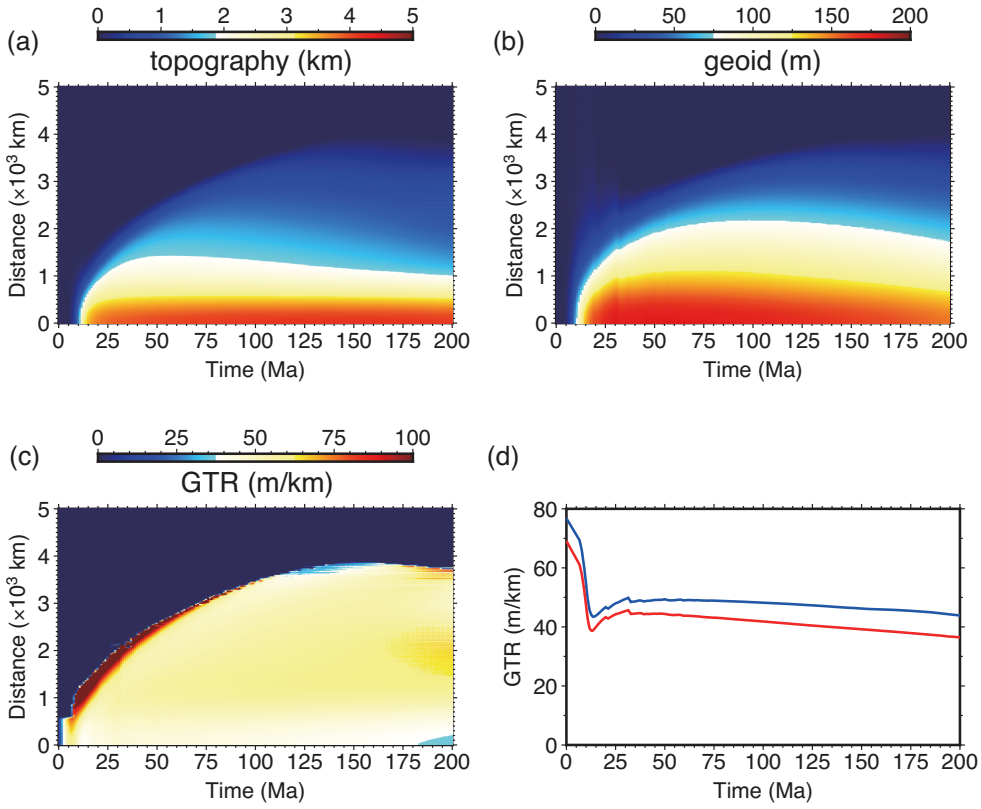

Figure 5. Parts (a)–(c) are dynamic topography, geoid anomaly and GTR as a function of time and distance from the plume centre point, respectively. Note that in (c), we only consider area with topography larger than 100 m to avoid unusually large GTR caused by small fluctuation of topography. (d) Time evolution of GTR at the centre point of the surface (red), and for area affected by plume–lithosphere interaction (blue), for example, the least-squares slope of geoid and topography at the surface for regions with topography larger than 100 m.

~15 times from ~0.01 to ~0.15 km^3 yr^{-1}. Interestingly, the melt production rate for the model with 400 km plume radius apparently decreases with time after it reaches a maximum, which is because small-scale convection quickly develops beneath the lithosphere and reduces the temperature of the previously melting region, resulting in reduced melt production rate. This has also been observed for the reference case at some later stage (e.g. >100 Ma), although the reduction is not as prominent (Fig. 7d, green curve).

3.2.2 *Effects of plume excess temperature*

In cases T1, T2 and T3 (Table 2), the plume excess temperature ΔT_p is changed to 350, 250 and 200 °C, respectively. The spatial variations of the dynamic topography, geoid anomaly and GTR for these cases are quite similar to case 1, except their magnitudes (Fig. 8), for example, the topography and geoid anomaly both decrease with increasing distance from the plume centre, while the GTR is smaller in the plume centre region than outside the plume centre. As shown in Fig. 9, a higher plume excess temperature produces a larger geoid anomaly (Fig. 9a), and a larger swell topography (Fig. 9b). When plume excess temperature is 350 °C, the geoid anomaly and topography both decrease after reaching their maximum in the first ~30 Ma (Figs 9a and b), due to the fast spreading of the plume beneath the lithosphere similar to a larger plume radius as discussed in Section 3.2.1. The influence of plume excess temperature on GTR is not dramatic, for example, the GTR is increased by ~5 m km^{-1} as the plume excess temperature increases from 200 °C to 300 °C (Fig. 9c).

The melt production rate increases dramatically with the increase of plume excess temperature (Fig. 9d). There is no melting extraction for plume excess temperature smaller than 200 °C (Fig. 9d). The total melt production increases by ~4 times from 0.3 to 1.2 km^3 yr^{-1} as the plume excess temperature increases from 300 °C to 350 °C (Fig. 9d). The melt production rate for plume excess temperature of 350 °C also decreases with time after reaching a maximum, due to the effects of small-scale convection quickly developed beneath the lithosphere (Fig. 9d).

3.2.3 *Effects of viscosity*

In cases L1, L2 and L3 (Table 2), we vary the activation energy for the lithosphere (e.g. top 100 km) E_l to 11.5, 9.21 and 4.61, respectively, and keep the activation energy for the mantle E_m (e.g. below 100 km depth) the same as the reference case ($E_m = 6.91$). This results in a maximum viscosity contrast across the lithosphere of 10^5 (for $E_l = 11.5$), 10^4 (for $E_l = 9.21$), 10^3 (for $E_l = 6.91$) and 10^2 (for $E_l = 4.61$), respectively. The spatial variations of the dynamic topography, geoid anomaly and GTR for cases with different lithosphere viscosity are similar (Fig. 10). For case with relatively smaller lithosphere viscosity, that is, $E_l = 4.61$, the GTR after ~150 Ma is rather heterogeneous in regions far away from the plume centre (Fig. 10), which is caused by the development of sublithosphere small-scale convection. The variation of lithospheric viscosity has no influence on the net geoid anomaly (Fig. 11a). The initial swell topography caused by plume–lithosphere interaction is nearly the same for different lithospheric viscosity before the plume starts to spread out

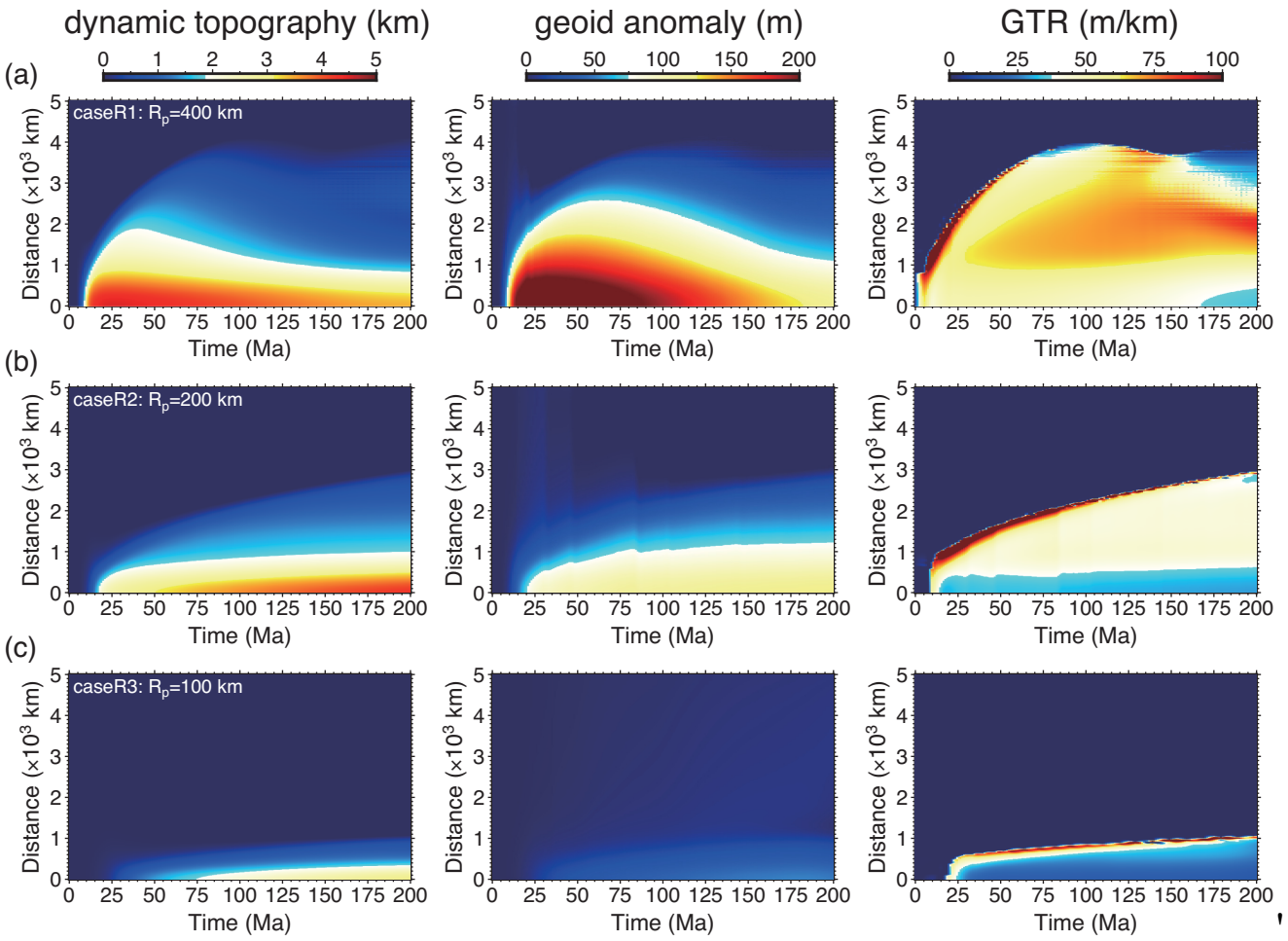

Figure 6. Time evolution of dynamic topography, geoid anomaly and GTR as a function of the distance from the plume centre for cases with different plume radius of (a) $R_p = 400$ km, (b) $R_p = 200$ km and (c) $R_p = 100$ km.

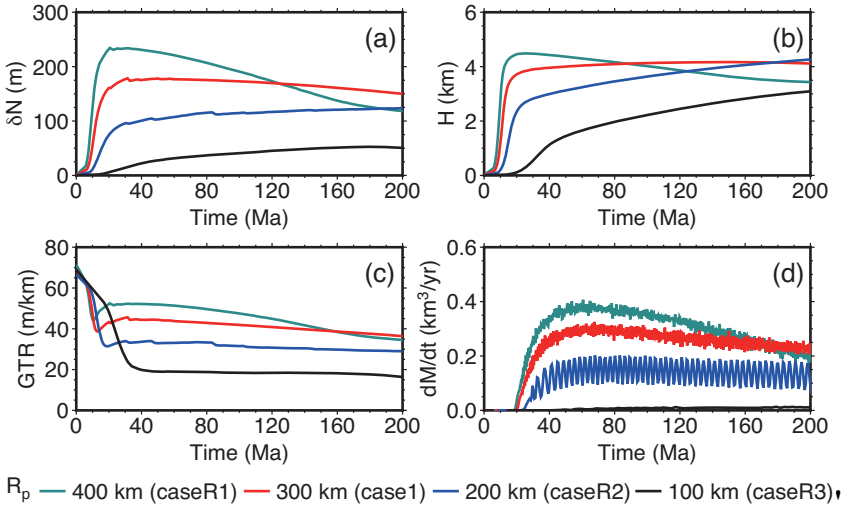

Figure 7. Time evolution of geoid anomaly (a), dynamic topography (b), GTR (c) and melt production rate (d), for models with different plume radius. In (a)–(c), the geoid anomaly, dynamic topography and GTR are calculated at the centre of the surface. In (d), the melt production rate is calculated by summing up the entire surface area.

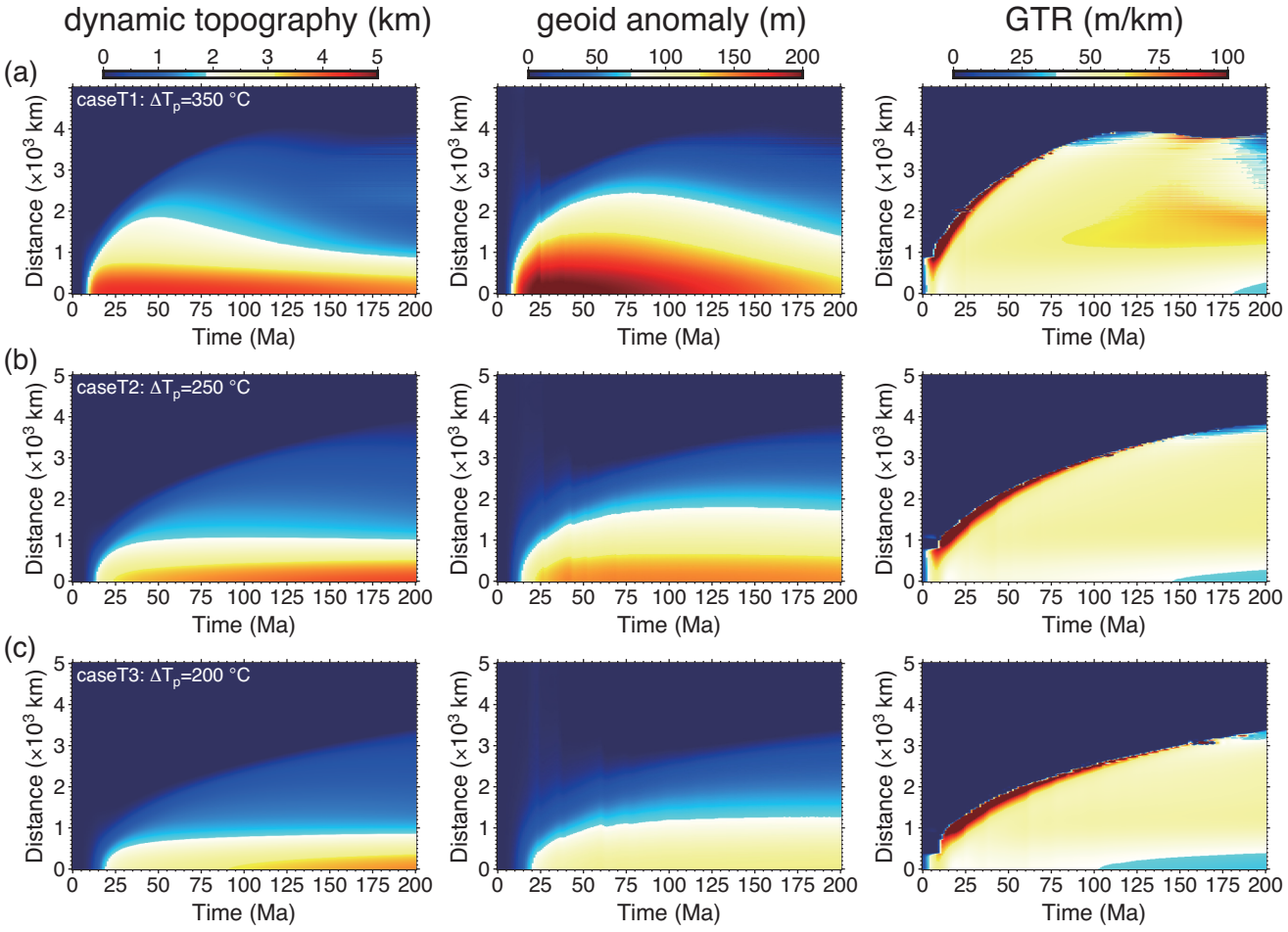

Figure 8. The same as Fig. 6, but for cases with different plume excess temperature ΔT_p.

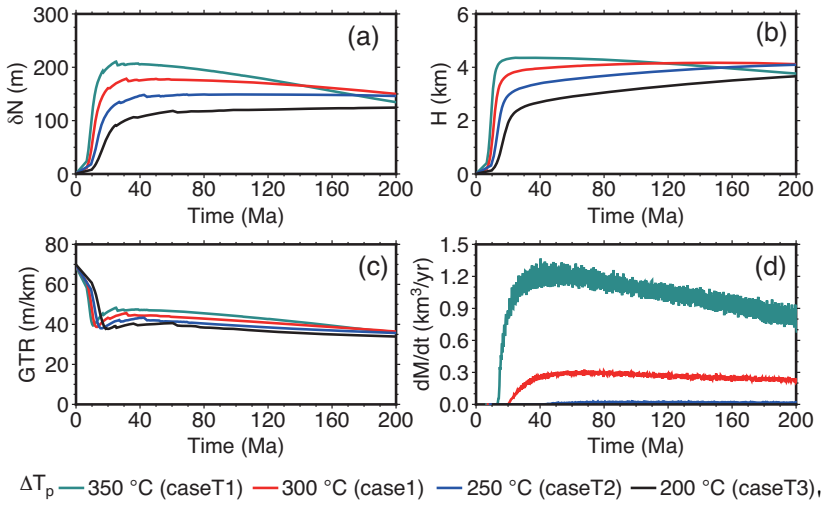

Figure 9. The same as Fig. 7, but for cases with different plume excess temperature ΔT_p.

(Fig. 11b, before ~30 Ma). After 30 Ma, a larger lithospheric viscosity produces a slightly smaller swell topography, but when the lithospheric viscosity contrast is larger than 10^3 (with $E_l = 6.91$) the variation of swell topography is not significant (Fig. 11b). The GTR is also not very sensitive to the lithospheric viscosity, for example, it varies by ~5 m km^{-1} as the lithospheric viscosity contrast varies from 10^2 to 10^5 (Fig. 11c). The melt production rate increases with the decrease of the lithospheric viscosity, especially when the lithospheric viscosity contrast is smaller than 10^3 (with $E_l = 6.91$, Fig. 11d). For example, the melt production rate increases from 0.15 to 0.3 km^3 yr^{-1} when the lithospheric viscosity contrast decreases from 10^4 to 10^3, and it increases up to ~0.8 km^3 yr^{-1} when the

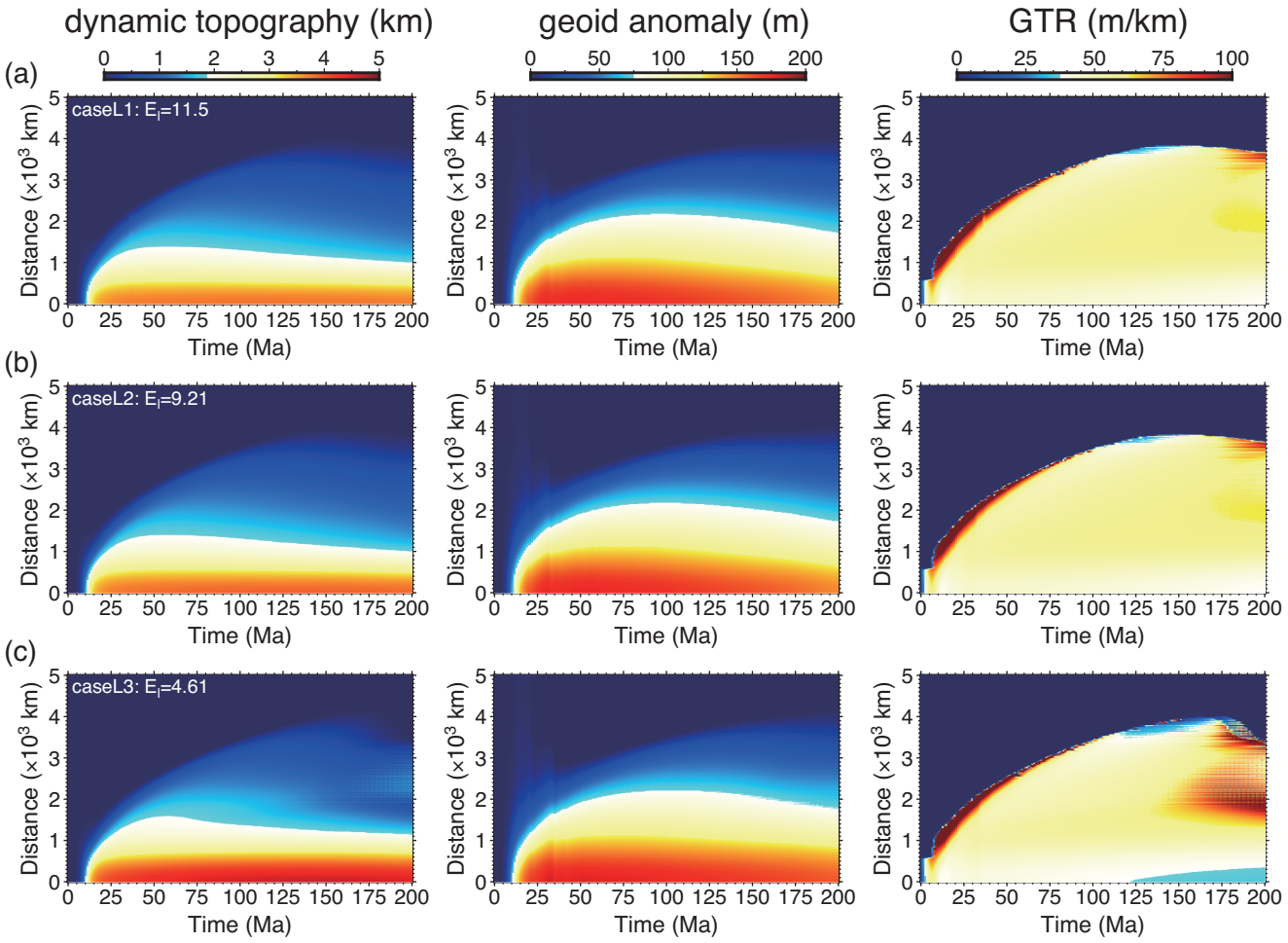

Figure 10. The same as Fig. 6, but for cases with different activation energy for the lithosphere E_l (e.g. top 100 km).

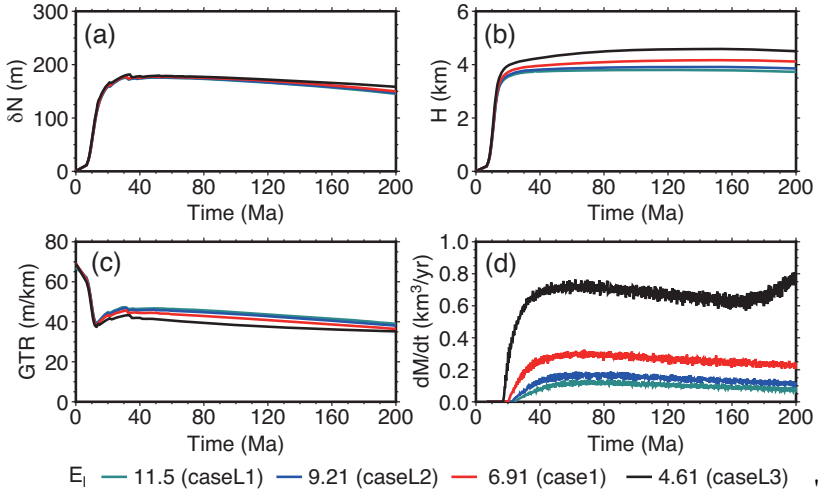

Figure 11. The same as Fig. 7, but for cases with different activation energy for the lithosphere E_l (e.g. top 100 km).

viscosity contrast decreases to 10^2 (with $E_l = 4.61$, Fig. 11d). It is worthy to point out that as the lithospheric viscosity contrast increase from 10^2 to 10^5, the interior of the lithosphere changes from being mobile to more stagnant. Limited by computational power, we do not test the effects of higher lithospheric viscosity contrast, but we expect them to be small since we find that the changes of geoid anomaly, dynamic topography and melt production rate are rather minor as we increase the lithospheric viscosity contrast from 10^4 to 10^5 (Fig. 11).

In cases P1, P2 and P3 (Table 2), we keep the activation energy of the lithosphere the same as the reference case (e.g. $E_l = 6.91$ for the top 100 km) and vary the activation energy of the mantle (e.g.

below 100 km depth) to E_m = 11.5, 9.21 and 4.61, respectively. This results in a maximum viscosity contrast between the plume and its surrounding mantle of 12.9 (E_m = 11.51), 7.7 (E_m = 9.21), 4.6 (E_m = 6.91) and 2.8 (E_m = 4.61), respectively. Note that a larger mantle activation energy results in smaller plume viscosity due to the high temperature of the plume. The spatial variations of the dynamic topography, geoid anomaly and GTR for these cases are similar to case 1, but a larger plume viscosity causes more homogeneous GTR (Fig. 12). A lower plume viscosity produces a slightly larger geoid anomaly at the early stage of plume–lithosphere interaction (Fig. 13a, before 30 Ma). However, the geoid anomaly decreases more rapidly after ∼30 Ma for smaller plume viscosity (Fig. 13a, red and green lines) due to its fast spreading rate of plume materials beneath the lithosphere, causing a lower geoid anomaly (or more homogeneous geoid) than other cases with higher plume viscosity after ∼80 Ma (Fig. 13a). The initial swell topography caused by plume–lithosphere interaction is nearly the same for different plume viscosity before the plume starts to spread out (Fig. 13b, before ∼30 Ma). After 30 Ma, a larger plume viscosity produces larger dynamic topography (Fig. 13b). The GTR slightly increases with the decrease of plume viscosity before ∼125 Ma but later decreases with the decrease of plume viscosity (Fig. 13c) due to the rapid decrease of geoid anomaly for models with smaller plume viscosity (Fig. 13a). The melt production rate generally increases with the increase of the plume viscosity (Fig. 13d).

In cases E1, E2 and E3 (Table 2), we vary the activation energy for both the lithosphere and the mantle simultaneously to 11.5, 9.21 and 4.61, respectively. Increasing the activation energy results in an increase of the lithospheric viscosity but a reduction of the plume viscosity. The spatial variations of the dynamic topography, geoid anomaly and GTR for these cases are similar to case 1 (Fig. 14). The variation of the geoid anomaly (Fig. 15a) is similar to Fig. 13(a), since lithospheric viscosity has little influence on geoid anomaly. A smaller activation energy E produces larger dynamic topography (Fig. 15b), because the decrease of lithospheric viscosity and the increase of plume viscosity both leads to increased dynamic topography, which in turn results in smaller GTR (Fig. 15c). The melt production rate increases with the decrease of E since the reduction of lithospheric viscosity and the increase of plume viscosity both enhance melt production rate (Fig. 15d).

3.2.4 Effects of lithosphere thickness

In cases A1, A2 and A3 (Table 2), we vary the lithospheric age A_l from 80 to 160 Ma, 120 and 60 Ma, which correspond to an initial lithosphere thickness D_l varying from 120 to 160 km, 140 and 100 km, respectively. The spatial variations of the dynamic topography, geoid anomaly and GTR for these cases are quite similar to case 1 (Fig. 16). Generally, a thicker lithosphere leads to slightly larger geoid anomaly and larger swell topography (Figs 17a and b). For example, as the lithosphere thickness increases from 100 to 160 km, the geoid anomaly is increased by ∼25 m and the dynamic topography is increased by ∼0.5 km (Figs 17a and b). The resulting GTRs are nearly identical for cases with different lithosphere thickness (Fig. 17c). Generally, a thinner lithosphere leads to a larger melt production rate (Fig. 17d). For initially thinner lithosphere (e.g. 100 km), the melt starts to produce and increases quickly after the plume reaches the base of the lithosphere, and the melt production rate subsequently decreases due to the thickening of the lithosphere (Fig. 17d). While for initially thicker lithosphere (e.g. 160 km), the melt production rate increases more slowly as the thick lithosphere is gradually thinned by the upwelling hot plume (Fig. 17d). The melt production rate tends to reach a same constant as long as the plume–lithosphere interaction reaches an equilibrium state with the same lithosphere thickness (Fig. 17d).

3.2.5 Effects of weak asthenosphere

The presence of a weak asthenosphere in the Earth's upper mantle has been suggested to be important in generating plate tectonics (Hoink *et al.* 2012) and also strongly affect the plume dynamics (Liu & Leng 2020a). However, this weak layer has been argued to be absent in other planet such as Venus which is characterized by stagnant-lid mantle convection (Huang *et al.* 2013). Here, we perform four cases considering a weak layer beneath the lithosphere in the upper mantle with different thickness d_w and viscosity reduction $\Delta\eta_w$. In cases W1–W4, the weak layer is set to d_w = 100 km and $\Delta\ \eta_w$= 0.1 for case W1, d_w = 300 km and $\Delta\ \eta_w$= 0.1 for case W2, d_w = 100 km and $\Delta\ \eta_w$= 0.01 for case W3, d_w = 300 km and $\Delta\ \eta_w$= 0.01 for case W4, respectively (Table 2). Generally, the spatial variations of the dynamic topography, geoid anomaly and GTR for cases W1–W2 are similar to case 1, but the pattern is much more complicated for cases W3 and W4 with a larger viscosity reduction of the weak layer for which vigorous small-scale convection is easily to develop due to the lower reduced viscosity (Fig. 18). The presence of the weak layer substantially reduces the geoid anomaly as well as the dynamic topography (Figs 19 a and b). The amplitudes of the geoid anomaly and dynamic topography decrease as the thickness or the viscosity reduction of the weak layer increases (Figs 19a and b), although there is a trade-off for the effects of the thickness and viscosity reduction (Figs 19a and b, blue line with d_w = 300 km $\Delta\ \eta_w$= 0.1 and black line with d_w = 100 km $\Delta\ \eta_w$= 0.01). However, the corresponding GTR does not change significantly, except for case W4 in which the geoid anomaly, dynamic topography and the GTR are all lower than cases W1–W3 (Fig. 19c). The presence of the weak layer significantly increases the melt production rate which is more dominantly controlled by the magnitude of the viscosity reduction of the weak layer than the thickness of the layer (Fig. 19d).

4 DISCUSSIONS

4.1 Sensitivities of surface expressions on model parameters

The dynamic topography, geoid anomaly and GTR above the plume centre and the total melt production rate are summarized in Table 2, in which the observables are averaged from 40 to 80 Ma for all cases to avoid (1) the effect of the initial impact stage of plume–lithosphere interaction and (2) the effect of side boundaries at a later stage. Among cases without weak layer, the maximum and minimum values of dynamic topography are observed in case E3 (4.54 km, R_p = 300 km, ΔT_p = 300 °C, $E_l = E_m$ = 6.91 and D_l = 120 km) and case R3 (1.46 km, R_p = 100 km, ΔT_p = 300 °C, $E_l = E_m$ = 6.91 and D_l = 120 km), respectively; the maximum and minimum values of geoid anomaly are observed in case R1 (200 m, R_p = 400 km, ΔT_p = 300 °C, $E_l = E_m$ = 6.91 and D_l = 120 km) and case R3 (27.9 m, R_p = 100 km, ΔT_p = 300 °C, $E_l = E_m$ = 6.91 and D_l = 120 km), respectively; the maximum and minimum values of GTR are observed in case E1 (52.4 m km^{-1}, R_p = 300 km, ΔT_p = 300 °C, $E_l = E_m$ = 11.5 and D_l = 120 km) and case R3 (19.2 m km^{-1}, R_p = 100 km, ΔT_p = 300 °C, $E_l = E_m$ = 6.91

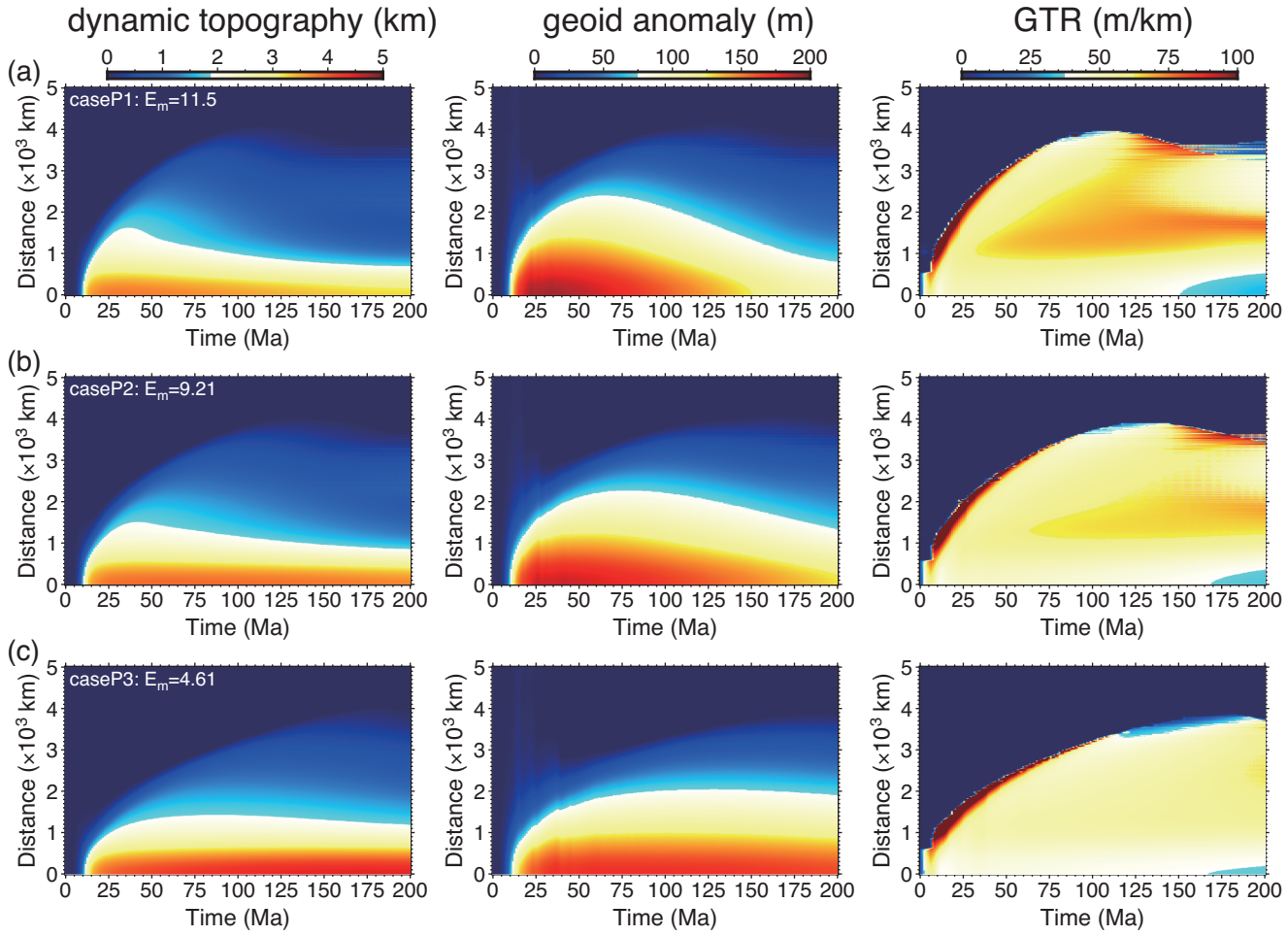

Figure 12. The same as Fig. 6, but for cases with different activation energy for the mantle E_m (e.g. below 100 km depth).

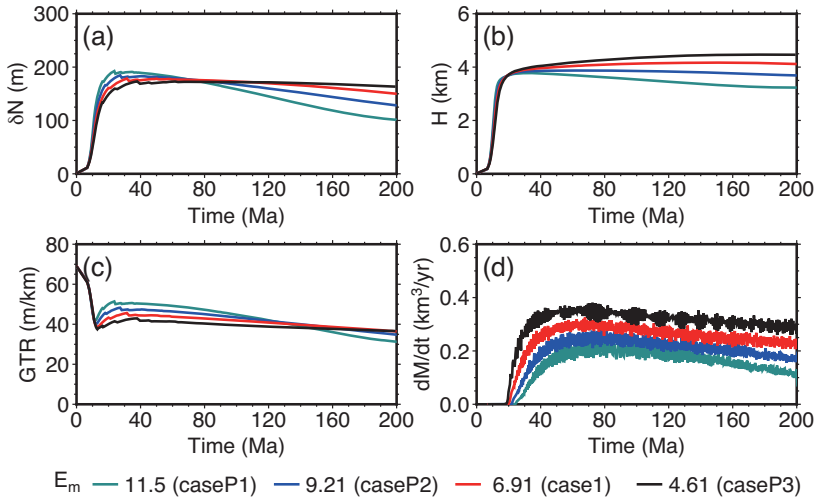

Figure 13. The same as Fig. 7, but for cases with different activation energy for the mantle E_m (e.g. below 100 km depth).

and $D_l = 120$ km), respectively; the maximum and minimum values of melt production rate are observed in case T1 (1.2 km^3 yr^{-1}, $R_p = 300$ km, $\Delta T_p = 350\,^\circ$C, $E_l = E_m = 6.91$ and $D_l = 120$ km) and case T3 with no melt production ($R_p = 300$ km, $\Delta T_p = 200\,^\circ$C, $E_l = E_m = 6.91$ and $D_l = 120$ km), respectively. With the presence of a weak layer, the minimum dynamic topography (1.3 km), minimum geoid anomaly (26.6 m), minimum GTR (20.3 m km^{-1}) and maximum melt production rate (12.14 km^3 yr^{-1}) are observed in case W4 ($R_p = 300$ km, $\Delta T_p = 300\,^\circ$C, $E_l = E_m = 6.91$, $D_l = 120$ km, $d_w = 300$ km and $\Delta\eta_w = 0.01$).

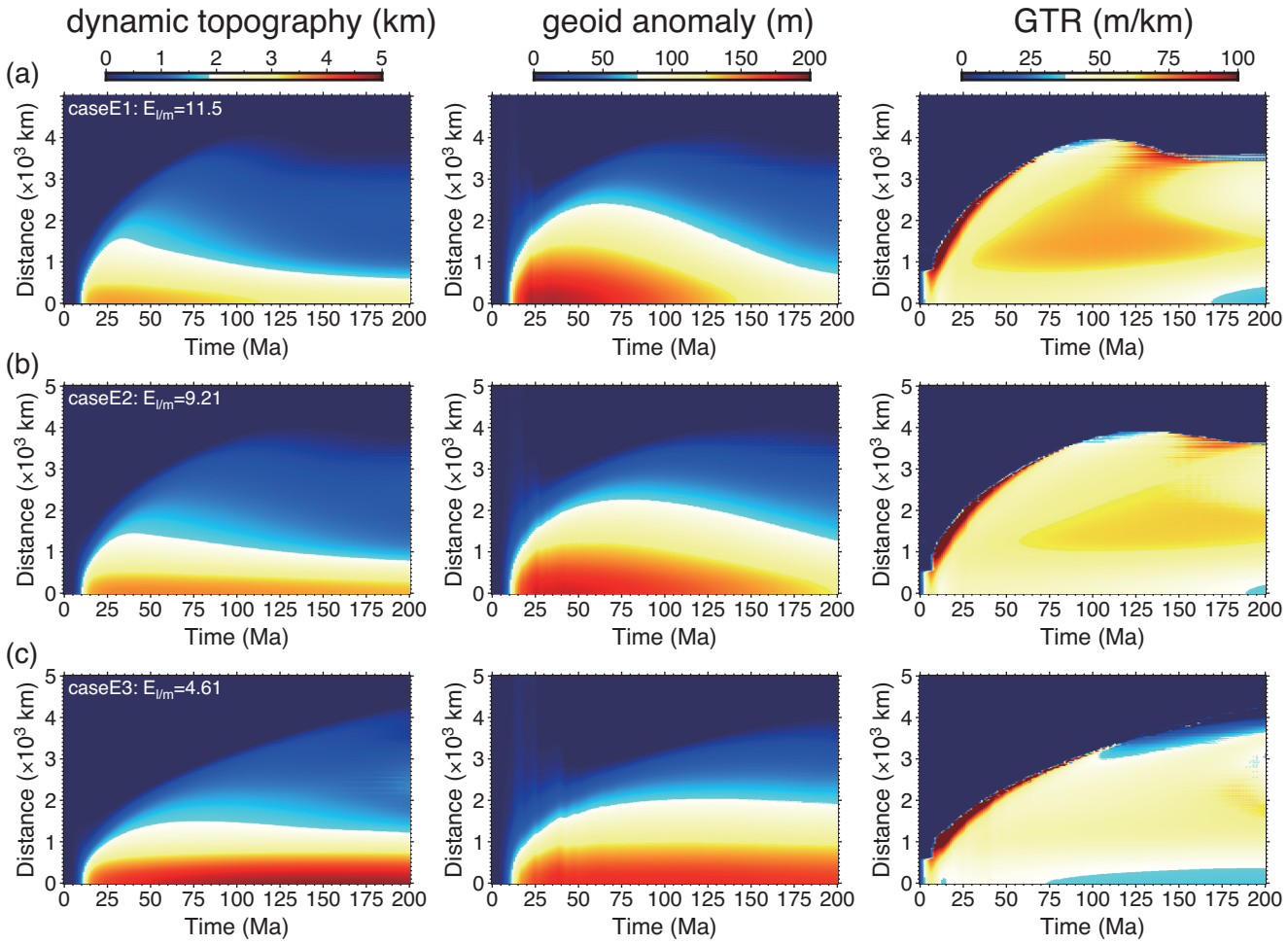

Figure 14. The same as Fig. 6, but for cases with different activation energy $E_{l/m}$.

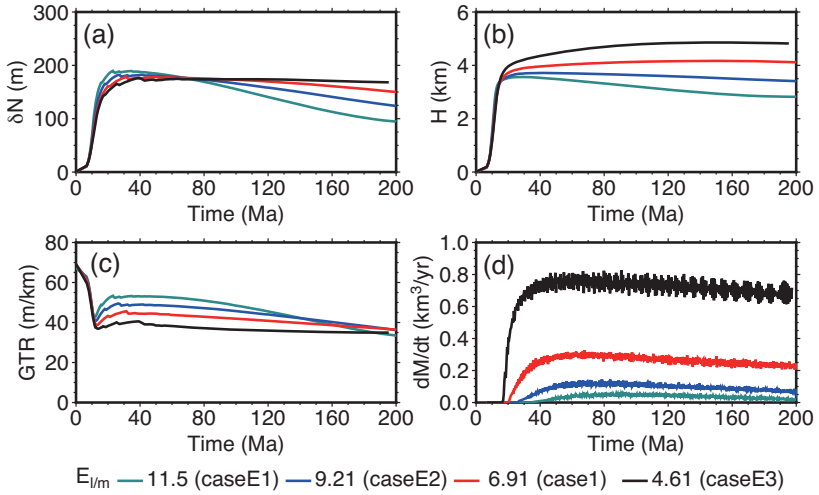

Figure 15. The same as Fig. 7, but for cases with different activation energy $E_{l/m}$.

Table 3 summarizes the sensitivities of surface observables to model parameters. Due to limits of computational time, the number of 3-D models we performed does not allow the derivation of robust scaling laws between the surface observables and model parameters. Instead, we focus on examining how the surface observables are sensitive to each model parameter at this stage. We find that the dynamic topography induced by the rising hot plume is strongly affected by plume radius and plume excess temperature with a positive correlation (Figs 7b and 9b). The viscosity of the lithosphere has little effect on dynamic topography, unless when the lithosphere is rather weak (Fig. 11b). This is consistent with the conclusions from previous studies on interaction of plume with

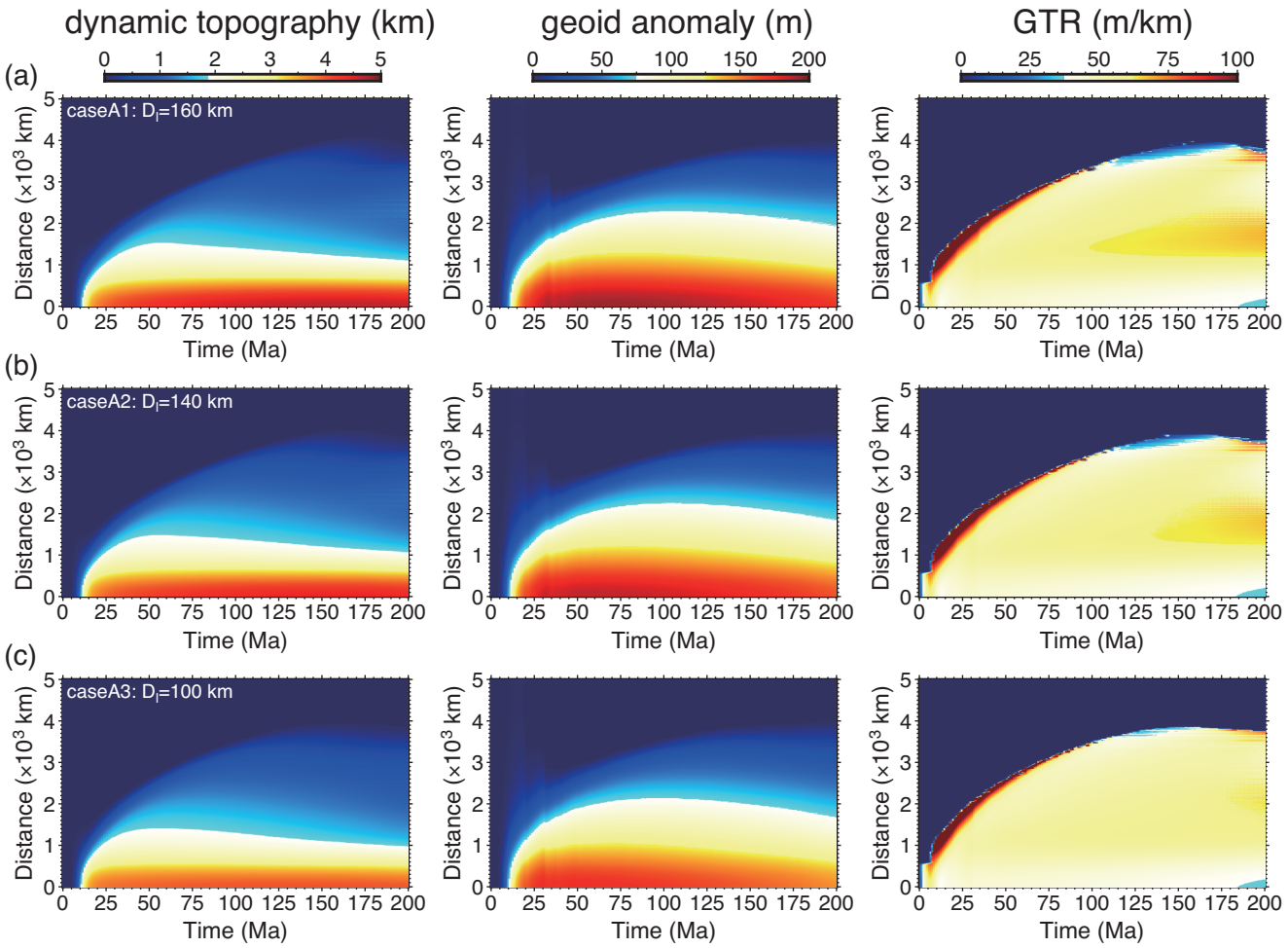

Figure 16. The same as Fig. 6, but for cases with different initial lithosphere thickness D_l.

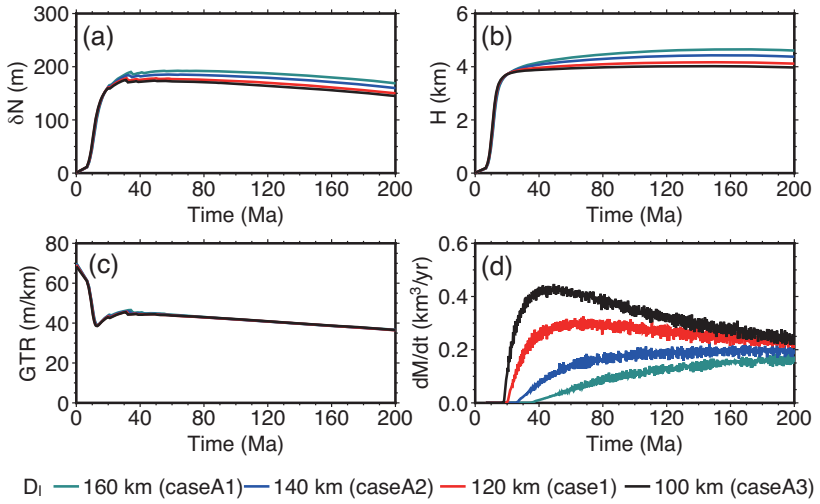

Figure 17. The same as Fig. 7, but for cases with different initial lithosphere thickness D_l.

a moving oceanic or continental lithosphere (Ribe & Christensen 1994; Yang & Leng 2014). The viscosity of the upwelling plume has a positive correlation with the topographic uplift on the surface (Fig. 13b). The lithosphere thickness has no significant effect on the dynamic topography (Fig. 17b).

The geoid anomaly is also strongly affected by the plume radius and the plume excess temperature with positive correlations (Figs 7a and 9a), because the contribution from the dynamic topography to the geoid anomaly is larger than the contribution of the internal density anomaly due to the plume. The lithospheric

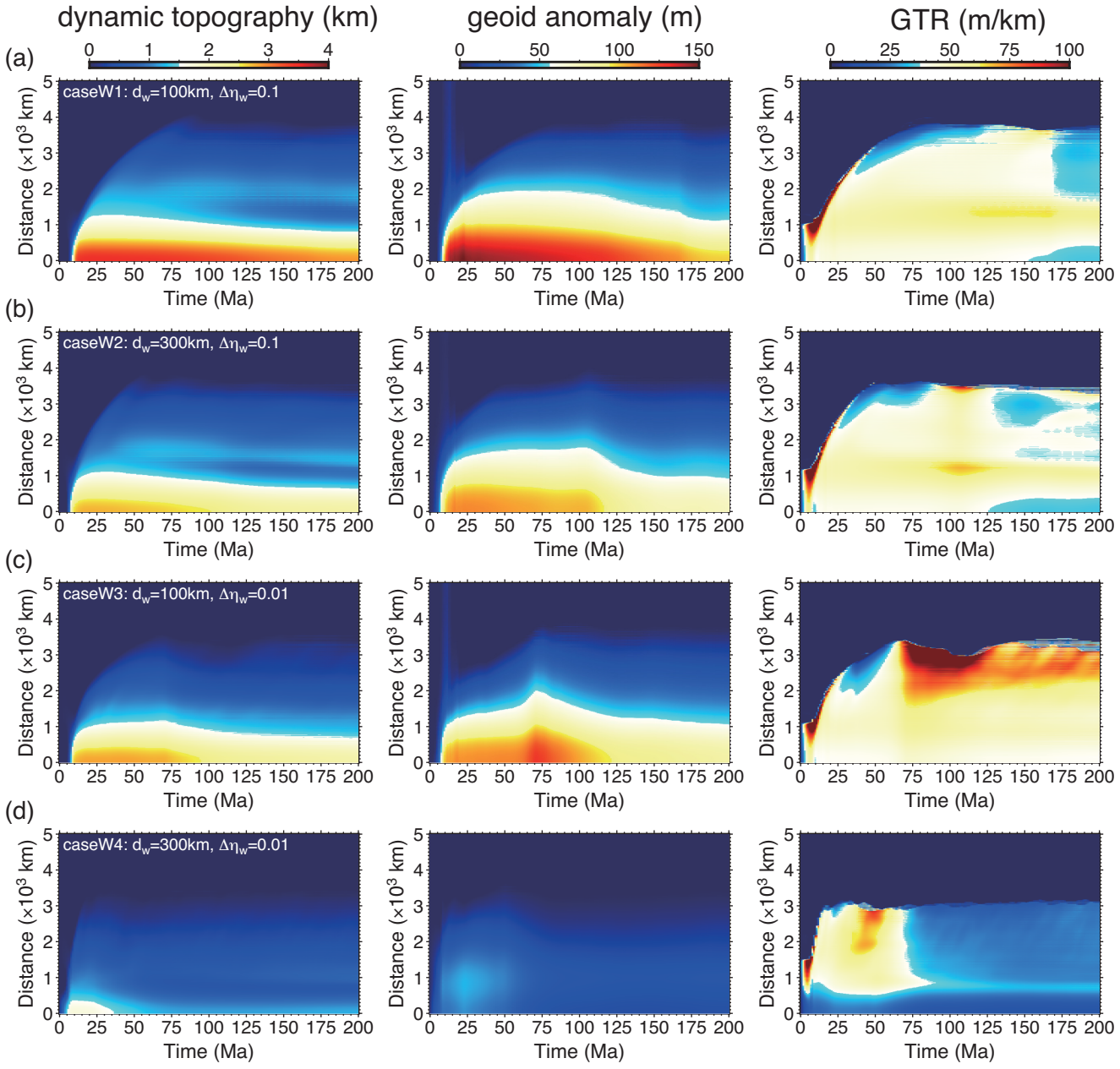

Figure 18. The same as Fig. 6, but for cases with a weak layer beneath the lithosphere.

viscosity has no influence on geoid anomaly since the topography is largely not affected (Fig. 11a), whereas the plume viscosity affects both the dynamic topography and the geoid anomaly (Fig. 13a). The lithospheric thickness has little effect on the geoid anomaly (Fig. 17a).

The GTR is more prominently influenced by the radius of the plume than the excess temperature of the plume (Figs 7c and 9c), although plume excess temperature also induces a large variation of dynamic topography and geoid anomaly. The GTR is more sensitive to the plume viscosity than the lithospheric viscosity (Figs 11c and 13c), due to the more significant influence of plume viscosity on dynamic topography and geoid anomaly. The lithospheric thickness has no significant influence on GTR (Fig. 17c).

The melt production rate is influenced by all model parameters, but the sensitivities are different. The excess temperature of the plume appears to affect the melt production rate more than the radius of the plume, though they both have significant positive influence on melt production rate (Figs 7d and 9d). The effect of lithospheric viscosity on melt production rate is not significant when the lithosphere is sufficiently strong, whereas the melt production rate is generally inversely correlated with the lithospheric viscosity when the lithosphere is relatively weak (Fig. 11d). The plume viscosity is generally positively correlated with the melt production rate, which is contrary to the effect of lithospheric viscosity (Fig. 13d). The melt production rate is also sensitive to the lithospheric thickness with an inverse correlation (Fig. 17d).

The presence of a weak viscosity layer, for example, the asthenosphere on Earth, also has significant influences on the surface expressions. The presence of the weak layer results in smaller geoid anomaly and dynamic topography, and the thicker or the weaker

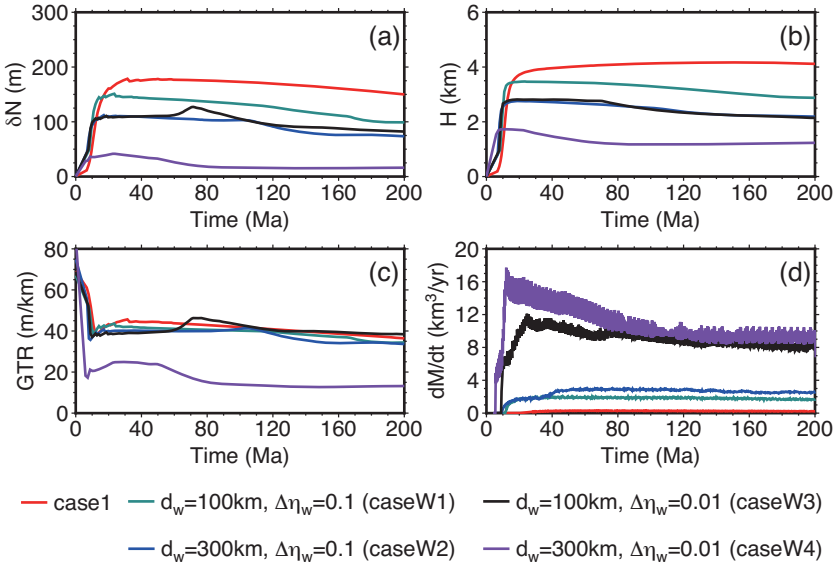

Figure 19. The same as Fig. 7, but for cases with a weak layer beneath the lithosphere.

Table 3. Sensitivity of surface observables to model parameters.

	Plume radius	*Plume excess temperature*	*Plume viscosity*	*Lithosphere viscosity*	*Lithosphere thickness*	*Weak asthenosphere*
Dynamic topography	H-P	H-P	M-P	W-N	W-P	H-P
Geoid anomaly	H-P	H-P	M-N	NOT	W-P	H-P
GTR	H-P	M-P	M-N	W-P	NOT	M-N
Melt production rate	H-P	H-P	M-P	M-N	H-N	H-P

H (green shading), M (yellow shading) and W (cyan shading) represent high, medium and weak sensitivity of observables on model parameters, respectively. P (blue) and N (red) represent positive and negative correlation of observables on model parameters, respectively. NOT indicates no effect of parameters on surface observables.

the layer the smaller the geoid anomaly and dynamic topography (Figs 19a and b). However, the corresponding GTR is not significantly influenced by the presence of the weak layer except when the layer is sufficiently thick and weak (e.g. 300 km thick and 100 times lower viscosity, Fig. 19c). The existence of the weak layer also induces larger melt production rate, and the magnitude of the viscosity reduction has more prominent influence on the melt production rate than the thickness of the weak layer (Fig. 19d).

4.2 Spatial and temporal variations of surface expressions

We found interesting spatial variations of the plume-induced dynamic topography, geoid anomaly and melt production rate. The dynamic topography is highest above the plume centre where the maximum excess temperature occurs and decreases with the distance away from the plume centre. The geoid anomaly has a similar spatial variation as the dynamic topography since the dynamic topography makes a larger contribution to the geoid anomaly than the interior density anomaly. The GTR, on the other hand, is more homogeneous but also shows some spatial differences, as the GTR in the plume centre region tends to be smaller than that in the region outside the centre. The melt production is always concentrated within the central part of the plume with no significant spatial variation. The pattern of these plume-induced observables places additional constraints on plume and lithosphere properties.

These plume-induced surface observables are also rather time-dependent. Before reaching the base of the lithosphere, the ascent of the mantle plume induces rapidly increased topographic uplift and positive geoid anomaly at the surface above the plume, while the GTR decreases rapidly from the initial stage. After the plume reaches the base of the lithosphere and then spreads out, the amplitude of the dynamic topography and geoid anomaly increases more slowly and becomes relatively stable after reaching the maximum values. On the other hand, the GTR decreases much more slowly after the plume head has flattened out at the base of the lithosphere. Melt is produced only after the plume reaches the base of the lithosphere, and the melt production rate first increases rapidly and then becomes relatively stable after it reaches its maximum value.

4.3 Implications for understanding plume–lithosphere interaction in planetary evolution

The geoid and topography have been modelled to investigate the interior structure of the mantle on Earth and other planets (e.g. Ribe & Christensen 1994; Zhong & Watts 2002; Roberts & Zhong 2004; Huang *et al.* 2013). However, previous studies have mostly focused on the steady state of the numerical modelling to compare with

the observational constraints. The time dependency of geoid and topography from our study implies that using a steady state cannot ideally constrain the plume or lithosphere properties if the timescale of the plume–lithosphere interaction is not well determined. A similar conclusion has also been reached by Kiefer & Kellogg (1998) using 2-D spherical axisymmetric models.

Tens of hotspots have been suggested to be related to active plumes on Venus (e.g. Ernst & Desnoyers 2004, and references therein). Beta, Atla and Western Eistla are three of these regions on Venus with different GTRs (31 m km^{-1} for Beta, 21 m km^{-1} for Alta and 20 m km^{-1} for Western Eistla) (Smrekar & Phillips 1991), and this difference has been interpreted to represent a range of evolutionary stages of plume–lithosphere interaction (Smrekar & Parmentier 1996). However, the difference of GTR may also indicate a difference in plume properties (e.g. size and excess temperature) due to its strong dependency on plume radius and plume temperature shown by our numerical results. The higher GTRs for Venusian hotspots comparing to that for Earth hotspots have been interpreted to indicate the absence of an Earth-like low-viscosity zone on Venus (Smrekar & Phillips 1991). However, our results show that the resultant GTR is only significantly reduced when the low-viscosity layer is enough wide and weak (e.g. 300 km thick and 100 times viscosity reduction, Fig. 12), suggesting that the existence of a relatively thin (e.g. 100 km) low-viscosity zone cannot be completely ruled out on Venus.

Here, we build a framework to explore the plume–lithosphere interaction and its surface expressions and we show how the surface expressions are sensitive to model parameters. It needs to be pointed out that we do not attempt to provide a quantitative comparison between these modelled observables and the real observations. The dynamic topography is not directly observable and to constrain it involves additional uncertainties (Molnar *et al.* 2015). In addition, there may be a significant part of gravity and topography from observations that are not associated with mantle convection, including the contribution from elastic lithospheric thickness or the surface loading of volcanic construction (e.g. Zhong 2002; Zhong & Roberts 2003; Roberts & Zhong 2004). In this study, we do not consider the effect of elastic lithospheric thickness which is expected to reduce the magnitude of the dynamic topography.

In addition to the elastic lithosphere deformation, there are other potential factors that affect the topography, gravity and melt production during plume–lithosphere interactions. Our numerical models use scaling parameters relative to the Earth. The surface temperature on Mars and Venus are much different than that on the Earth and may significantly influence the lithospheric viscosity structure. The rate of melt production is also very sensitive to the water content of the mantle (e.g. Katz *et al.* 2003; Hirschmann 2006; Till *et al.* 2010; Lees *et al.* 2020), the chemical structure of the lithosphere (e.g. Smrekar & Parmentier 1996; O'Neill *et al.* 2005; Manglik & Christensen 2006) and the mantle potential temperature (e.g. Nimmo & McKenzie 1996; Katz *et al.* 2003; Till *et al.* 2010). In addition, we assume all melts, once produced, are instantaneously extracted to the surface, but in reality, some melts may be intrusive and frozen beneath the surface. The extraction of melts depletes the melting regions in volatiles and thus may increase the viscosity in these regions, which we did not consider in our models. We also did not consider situations when the surface plate moves, which have been shown by previous studies to greatly affect the pattern of the plume-induced observables (e.g. Ribe & Christensen 1994; Ribe & Christensen 1999; Yang & Leng 2014; Liu & Leng 2020b, Connolly *et al.* 2009). More complexities can be included in our models for the purpose of a more quantitative comparison with observations in future work.

5 CONCLUSION

We perform numerical experiments to investigate the influence of plume radius, plume excess temperature, plume viscosity, lithospheric viscosity and lithospheric thickness on time evolution of plume-induced surface dynamic topography, geoid anomaly and melt production rate. A new method is incorporated into the CitcomCU code to calculate geoid anomaly in regional models. We test different values of plume radius (100–400 km), plume excess temperature (200–350 °C), plume viscosity (minimum value of 7.7 $\times$ 10^{19}–3.6 $\times$ 10^{20} Pa·s), lithosphere viscosity (maximum value of 1.0 $\times$ 10^{23}–1.0 $\times$ 10^{26} Pa·s), lithosphere thickness (100–160 km) and the presence of weak asthenosphere (thickness of 100–300 km, viscosity reduction of 10–100 times). Our experiments show that the geoid anomaly, dynamic topography, GTR and melt production, are strongly controlled by physical properties of the plume and the lithosphere, but the sensitivities of these surface expressions to plume and lithosphere properties are different.

The geoid anomaly is more sensitive (with positive correlation) to plume radius and plume excess temperature but less sensitive to plume viscosity (negatively correlated) and lithospheric thickness (positively correlated), and not sensitive to lithospheric viscosity. The dynamic topography is more sensitive (with positive correlation) to plume radius, plume excess temperature and plume viscosity but is less sensitive to lithospheric viscosity (negatively correlated) and thickness (positively correlated). The GTR is more sensitive to plume radius (positive correlation) but less sensitive to plume excess temperature (positive correlation) and plume viscosity (negative correlation) and is nearly not sensitive to lithospheric viscosity and thickness. The melt production rate is sensitive to all the plume and lithosphere properties with positive correlation to plume radius, plume excess temperature, plume viscosity and negative correlation to lithospheric viscosity and thickness.

We also find significant temporal and spatial variations of the plume-induced surface expressions. Before reaching the base of the lithosphere, the ascent of a mantle plume causes positive and rapid increase of dynamic topography and geoid anomaly at the surface but no melt production. The subsequent impinging of a plume head to the base of the lithosphere leads to further increase of dynamic topography and geoid anomaly and rapid increase of melt production. As the plume head spreads out beneath the lithosphere, these plume-induced observables reach maximum values and become relatively stable, except that the development of small-scale convection near the edges of the plume head leads to slight decrease of dynamic topography and geoid anomaly above these regions. Whereas the geoid anomaly and dynamic topography decrease from regions above the plume centre to regions above the plume edge, the melt production keeps concentrating at the centre part of the plume. The GTR is more spatially homogeneous but has a relatively smaller amplitude above the central parts of the plume, and it first decreases rapidly during the rising and impinging of a plume head to the base of the lithosphere and decreases more slowly after the plume head has spread out beneath the lithosphere.

ACKNOWLEDGEMENTS

We thank B. Steinberger and an anonymous reviewer and Editor Gaël Choblet for their insightful and constructive review and

comments that significantly improve the paper. The work is supported by NSF grant EAR-1849949 and EAR-1855624. The geodynamic models were performed on the Agave supercomputer at Arizona State University. Fig. 1 was generated with ParaView (http://www.paraview.org) and the rest of the figures were drawn using the Generic Mapping Tools (GMT, www.soest.hawaii.edu/gmt/). The modified CitcomCU code used in this study is available from the corresponding author upon request.

REFERENCES

Burov, E. & Gerya, T., 2014. Asymmetric three-dimensional topography over mantle plumes, *Nature,* **513,** 85–89.

Campbell, I.H. & Griffiths, R.W., 1990. Implications of mantle plume structure for the evolution of flood basalts, *Earth planet. Sci. Lett.,* **99,** 79–93.

Campbell, I.H. & Kerr, A.C., 2007. The great plume debate: testing the plume theory, *Chem. Geol.,* **241,** 149–152.

Citron, R.I., Manga, M. & Tan, E., 2018. A hybrid origin of the Martian crustal dichotomy: degree-1 convection antipodal to a giant impact, *Earth planet. Sci. Lett.,* **491,** 58–66.

Condie, K.C., 1998. Episodic continental growth and supercontinents: a mantle avalanche connection? *Earth planet. Sci., Lett.,* **163,** 97–108.

Condie, K.C., 2001. *Mantle Plumes and their Record in Earth History,* , Cambridge University Press, Cambridge.

Connolly, J.A.D., Schmidt, M.W., Solferino, G. & Bagdassarov, N., 2009. Permeability of asthenospheric mantle and melt extraction rates at mid-ocean ridges, *Nature,* **462,** 209–212.

d'Acremont, E., Leroy, S. & Burov, E.B., 2003. Numerical modelling of a mantle plume: the plume head-lithosphere interaction in the formation of an oceanic large igneous province, *Earth planet. Sci. Lett.,* **206,** 379–396.

Davaille, A., Smrekar, S.E. & Tomlinson, S., 2017. Experimental and observational evidence for plume-induced subduction on Venus, *Nat. Geosci.,* **10,** 349–355.

Davies, G.F., 2001. Dynamic earth: plates, plumes and mantle convection, *Am. J. Phys.,* **69,** 620–621.

Ernst, R.E. & Desnoyers, D.W., 2004. Lessons from Venus for understanding mantle plumes on Earth, *Phys. Earth planet. Inter.,* **146,** 195–229.

Farnetani, C.G. & Richards, M.A., 1994. Numerical investigations of the mantle plume initiation model for flood-basalt events, *J. geophys. Res. [Solid Earth],* **99,** 13813–13833.

Forsyth, D.W., Webb, S.C., Dorman, L.M. & Shen, Y., 1998. Phase velocities of Rayleigh waves in the MELT experiment on the East Pacific Rise, *Science,* **280,** 1235–1238.

French, S.W. & Romanowicz, B., 2015. Broad plumes rooted at the base of the Earth'smantle beneath major hotspots, *Nature,* **525,** 95–99.

Hager, B.H. & Richards, M.A., 1989. Long-wavelength variations in Earths geoid—physical models and dynamical implications, *Philos. Trans. R. Soc. A,* **328,** 309–327.

Hansen, V.L., 2002. Artemis: surface expression of a deep mantle plume on Venus, *Bull. geol. Soc. Am.,* **114,** 839–848.

Harder, H., 2000. Mantle convection and the dynamic geoid of Mars, *Geophys. Res. Lett.,* **27,** 301–304.

Harder, H. & Christensen, U.R., 1996. A one-plume model of martian mantle convection, *Nature,* **380,** 507–509.

Hirschmann, M.M., 2006. Water, melting, and the deep earth H2O cycle, *Annu. Rev. Earth Planet. Sci.,* **34,** 629–653.

Hoink, T., Lenardic, A. & Richards, M., 2012. Depth-dependent viscosity and mantle stress amplification: implications for the role of the asthenosphere in maintaining plate tectonics, *Geophys. J. Int.,* **191,** 30–41.

Huang, J.S., Yang, A. & Zhong, S.J., 2013. Constraints of the topography, gravity and volcanism on Venusian mantle dynamics and generation of plate tectonics, *Earth planet. Sci. Lett.,* **362,** 207–214.

Katz, R.F., Spiegelman, M. & Langmuir, C.H., 2003. A new parameterization of hydrous mantle melting, *Geochem. Geophys. Geosyst.,* **4,** doi:10.1029/2002gc000433.

Keller, T. & Tackley, P.J., 2009. Towards self-consistent modeling of the martian dichotomy: the influence of one-ridge convection on crustal thickness distribution, *Icarus,* **202,** 429–443.

Kiefer, W.S., 2003. Melting in the martian mantle: Shergottite formation and implications for present-day mantle convection on Mars, *Meteorit. Planet. Sci.,* **38,** 1815–1832.

Kiefer, W.S. & Hager, B.H., 1991. A mantle plume model for the equatorial highlands of venus, *J. geophys. Res.—Planet,* **96,** 20947–20966.

Kiefer, W.S. & Hager, B.H., 1992. Geoid anomalies and dynamic topography from convection in cylindrical geometry - applications to mantle plumes on earth and venus, *Geophys. J. Int.,* **108,** 198–214.

Kiefer, W.S. & Kellogg, L.H., 1998. Geoid anomalies and dynamic topography from time-dependent, spherical axisymmetric mantle convection, *Phys. Earth planet. Inter.,* **106,** 237–256.

King, S.D. & Adam, C., 2014. Hotspot swells revisited, *Phys. Earth planet. Inter.,* **235,** 66–83.

Lees, M.E., Rudge, J.F. & McKenzie, D., 2020. Gravity, topography, and melt generation rates from simple 3-D models of mantle convection, *Geochem. Geophys. Geosyst.,* **21,** e2019GC008809, doi:10.1029/2019GC008809.

Li, M.M., Black, B., Zhong, S.J., Manga, M., Rudolph, M.L. & Olson, P., 2016. Quantifying melt production and degassing rate at mid-ocean ridges from global mantle convection models with plate motion history, *Geochem. Geophys. Geosyst.,* **17,** 2884–2904.

Li, M.M., McNamara, A.K. & Garnero, E.J., 2014. Chemical complexity of hotspots caused by cycling oceanic crust through mantle reservoirs, *Nat. Geosci.,* **7,** 366–370.

Li, Q. & Kiefer, W.S., 2007. Mantle convection and magma production on present-day Mars: effects of temperature-dependent rheology, *Geophys. Res. Lett.,* **34,** doi:10.1029/2007GL030544.

Liu, H. & Leng, W., 2020a. Plume-tree structure induced by low-viscosity layers in the upper mantle, *Geophys. Res. Lett.,* **47,** doi:10.1029/2019GL086508.

Liu, H. & Leng, W., 2020b. Tarim large igneous province caused by a wide and wet mantle plume, *J. geophys. Res. [Solid Earth],* **125,** e2019JB019001, doi:10.1029/2019JB019001.

Manglik, A. & Christensen, U.R., 2006. Effect of lithospheric root on decompression melting in plume–lithosphere interaction models, *Geophys. J. Int.,* **164,** 259–270.

Molnar, P., England, P.C. & Jones, C.H., 2015. Mantle dynamics, isostasy, and the support of high terrain, *J. geophys. Res. [Solid Earth],* **120,** 1932–1957.

Montelli, R., Nolet, G., Dahlen, F.A. & Masters, G., 2006. A catalogue of deep mantle plumes: new results from finite-frequency tomography, *Geochem. Geophys. Geosyst.,* **7,** doi:10.1029/2006GC001248.

Morgan, W.J., 1971. Convection plumes in lower mantle, *Nature,* **230,** 42–43.

Morgan, W.J., 1972. Deep mantle convection plumes and plate motions, *Am. Assoc. Petrol. Geol. B,* **56,** 203–213.

Navrotsky, A., 1995. Thermodynamic properties of minerals, *Miner. Phys. Crystallogr.,* doi:10.1029/RF002p0018.

Nelson, P.L. & Grand, S.P., 2018. Lower-mantle plume beneath the Yellowstone hotspot revealed by core waves, *Nat. Geosci.,* **11,** 280–284.

Nimmo, F. & McKenzie, D., 1996. Modelling plume-related uplift, gravity and melting on Venus, *Earth planet. Sci. Lett.,* **145,** 109–123.

O'Neill, C., Moresi, L. & Lenardic, A., 2005. Insulation and depletion due to thickened crust: effects on melt production on Mars and Earth, *Geophys. Res. Lett.,* **32,** doi:10.1029/2005GL022855.

Phillips, R.J., 1994. Estimating lithospheric properties at atla regio, venus, *Icarus,* **112,** 147–170.

Ribe, N.M. & Christensen, U.R., 1994. 3-dimensional modeling of plume-lithosphere interaction, *J. geophys. Res. [Solid Earth],* **99,** 669–682.

Ribe, N.M. & Christensen, U.R., 1999. The dynamical origin of Hawaiian volcanism, *Earth Planet. Sci., Lett.,* **171,** 517–531.

Richards, M.A., Duncan, R.A. & Courtillot, V.E., 1989. Flood basalts and hot-spot tracks—plume heads and tails, *Science,* **246,** 103–107.

Richards, M.A. & Hager, B.H., 1984. Geoid anomalies in a dynamic Earth, *J. geophys. Res.,* **89,** 5987–6002.

Roberts, J.H. & Zhong, S.J., 2004. Plume-induced topography and geoid anomalies and their implications for the Tharsis rise on Mars, *J. geophys. Res.—Planet,* **109,** doi:10.1029/2003je002226.

Roberts, J.H. & Zhong, S.J., 2006. Degree-1 convection in the Martian mantle and the origin of the hemispheric dichotomy, *J. geophys. Res.—Planet,* **111,** doi:10.1029/2005je002668.

Saffman, P.G. & Taylor, G.I., 1958. The penetration of a fluid into a porous medium or Hele-Shaw cell containing a more viscous liquid, *Proc. R. Soc. Lond. Ser. A. Math. Phys. Sci.,* **245,** 312–329.

Smrekar, S.E., 1994. Evidence for active hotspots on Venus from analysis of magellan gravity data, *Icarus,* **112,** 2–26.

Smrekar, S.E., Davaille, A. & Sotin, C., 2018. Venus interior structure and dynamics, *Space Sci. Rev*., **214,** doi:10.1007/s11214-018-0518-1.

Smrekar, S.E. & Parmentier, E.M., 1996. The interaction of mantle plumes with surface thermal and chemical boundary layers: applications to hotspots on Venus, *J. geophys. Res. [Solid Earth],* **101,** 5397–5410.

Smrekar, S.E. & Phillips, R.J., 1991. Venusian highlands—geoid to topography ratios and their implications, *Earth planet. Sci. Lett.,* **107,** 582–597.

Spiegelman, M. & McKenzie, D., 1987. Simple 2-D models for melt extraction at Midocean Ridges and Island Arcs, *Earth planet. Sci., Lett.,* **83,** 137–152.

Šrámek, O. & Zhong, S., 2012. Martian crustal dichotomy and Tharsis formation by partial melting coupled to early plume migration, *J. geophys. Res.: Planets,* **117,** doi:10.1029/2011JE003867.

Till, C.B., Elkins-Tanton, L.T. & Fischer, K.M., 2010. A mechanism for low-extent melts at the lithosphere-asthenosphere boundary, *Geochem. Geophys. Geosyst.,* **11,** doi:10.1029/2010GC003234.

Yang, T. & Leng, W., 2014. Dynamics of hidden hotspot tracks beneath the continental lithosphere, *Earth planet. Sci., Lett.,* **401,** 294–300.

Zhong, S.J., 2002. Effects of lithosphere on the long-wavelength gravity anomalies and their implications for the formation of the Tharsis rise on Mars, *J geophys Res.—Planet,* **107,** doi:10.1029/2001je001589.

Zhong, S.J., 2006. Constraints on thermochemical convection of the mantle from plume heat flux, plume excess temperature, and upper mantle temperature, *J. geophys. Res. [Solid Earth],* **111,** doi:10.1029/2005jb003972.

Zhong, S.J., 2009. Migration of Tharsis volcanism on Mars caused by differential rotation of the lithosphere, *Nat Geosci,* **2,** 19–23.

Zhong, S.J., Gurnis, M. & Hulbert, G., 1993. Accurate determination of surface normal stress in viscous-flow from a consistent boundary flux method, *Phys. Earth planet. Inter.,* **78,** 1–8.

Zhong, S.J., McNamara, A., Tan, E., Moresi, L. & Gurnis, M., 2008. A benchmark study on mantle convection in a 3-D spherical shell using CitcomS, *Geochem. Geophys. Geosyst.,* **9,** doi:10.1029/2008gc002048.

Zhong, S.J. & Roberts, J.H., 2003. On the support of the Tharsis Rise on Mars, *Earth planet. Sci. Lett.,* **214,** 1–9.

Zhong, S.J. & Watts, A.B., 2002. Constraints on the dynamics of mantle plumes from uplift of the Hawaiian Islands, *Earth planet. Sci. Lett.,* **203,** 105–116.